for axonal regeneration. Interestingly, the number, length, and diameter of the vessels have been reported to reach their maximum within 1 week after SCI, and vessels with abnormally large lumina may represent newly formed vessels after SCI (Casella et al., 2002). In the present study, we showed that the introduction of HGF into the injured spinal cord increased the total area of RECA-1-positive endothelial cells and number of vessels with abnormally large lumina by 1 week after SCI, confirming that HGF also promoted angiogenesis during the acute phase of SCI. Because HGF simultaneously stimulates the migration of endothelial cells and VSMCs (Nakamura et al., 1995, 1996), blood vessels might mature in a well-coordinated way, without the release of inflammatory cells (Morishita et al., 2004). Consistently with this suggestion, HGF overexpression reduced cerebral ischemic injury, without causing cerebral edema, through angiogenic and neuroprotective actions (Shimamura et al., 2004). Taken together, our results suggest that HGF may promote angiogenesis without enhancing blood vessel permeability after SCI and contribute to a reduction in the area of damage and regeneration of the injured spinal cord.

Several researchers have reported that HGF plays a role as an axonal chemoattractant and enhances the axonal growth of motoneurons (Ebens et al., 1996; Wong et al., 1997; Caton et al., 2000) and cortical neurons (Yamagata et al., 1995). Furthermore, it has been reported that overexpression of HGF in the chronic stage of cerebral infarction enhances neurite extension and increases the number of synapses, leading to improvements in learning and memory (Shimamura et al., 2006). In the present study, we demonstrated that HGF significantly induced the regrowth of raphe-spinal 5HT-positive fibers, which are known to contribute to the locomotor functions after SCI in rats (Bregman, 1987; Saruhashi et al., 1996; Kim et al., 2004; Kaneko et al., 2006), and the fibers expressed GAP-43 at 6 weeks after SCI. Moreover, c-Met-IR was also detected in the 5HT-positive fibers, suggesting that HGF directly acted on these fibers as well as the neuronal bodies to promote axonal regrwoth and recovery of locomotor functions after SCI. On the other hand, most of the longitudinal RT97-positive fibers oriented parallel to each other (Fig. 7G) did not express GAP-43 but expressed c-Met (Fig. 7J). Because these RT97-positive fibers were observed more abundantly in the HGF group than in the LacZ group at 6 weeks after SCI (Fig. 7H), it is likely that HGF protected the axons from degeneration.

Overall, during the acute phase of SCI, HGF appears to exert significant neuroprotective and antiapoptotic effects, to promote the survival of neurons and oligodendrocytes, and also to enhance angiogenesis around the lesion epicenter after SCI. These effects significantly reduced the area of damage and provided a better scaffold for axonal regeneration. Furthermore, HGF directly acted on the 5HT-positive fibers to promote their regrowth, which likely contributed to the significantly better recovery of the motor functions during the chronic phase of SCI. In conclusion, we have demonstrated that HGF exerted multiple beneficial effects on the injured spinal cord and significantly enhanced endogenous repair after SCI.

ACKNOWLEDGMENTS

We thank Seiji Okada and Hiroyuki Kato for critical review of the manuscript, Tokuko Harada for tender animal care, and Sachiyo Miyao for technical assistance.

REFERENCES

Beattie MS, Bresnahan JC, Komon J, Tovar CA, Van Meter M, Anderson DK, Faden AI, Hsu CY, Noble LJ, Salzman S, Young W. 1997. Endogenous repair after spinal cord contusion injuries in the rat. Exp Neurol 148:453–463.

Blesch A, Tuszynski MH. 2001. GDNF gene delivery to injured adult CNS motor neurons promotes axonal growth, expression of the trophic neuropeptide CGRP, and cellular protection. J Comp Neurol 436:399–410.

Bottaro DP, Rubin JS, Faletto DL, Chan AM, Kmiecik TE, Vande Woude GF, Aaronson SA. 1991. Identification of the hepatocyte growth factor receptor as the c-met protooncogene product. Science 251:802–804.

Bregman BS. 1987. Spinal cord transplants permit the growth of serotonergic axons across the site of neonatal spinal cord transection. Brain Res 431:265–279.

Casella GT, Marcillo A, Bunge MB, Wood PM. 2002. New vascular tissue rapidly replaces neural parenchyma and vessels destroyed by a contusion injury to the rat spinal cord. Exp Neurol 173:63–76.

Caton A, Hacker A, Naeem A, Livet J, Maina F, Bladt F, Klein R, Birchmeier C, Guthrie S. 2000. The branchial arches and HGF are growth-promoting and chemoattractant for cranial motor axons. Development 127:1751–1766.

Coffin RS, Thomas SK, Thomas DP, Latchman DS. 1998. The herpes simplex virus 2 kb latency associated transcript (LAT) leader sequence allows efficient expression of downstream proteins which is enhanced in neuronal cells: possible function of LAT ORFs. J Gen Virol 79:3019–3026.

Date I, Takagi N, Takagi K, Kago T, Matsumoto K, Nakamura T, Takeo S. 2004. Hepatocyte growth factor improved learning and memory dysfunction of microsphere-embolized rats. J Neurosci Res 78:442–453.

Ebens A, Brose K, Leonardo ED, Hanson MG Jr, Bladt F, Birchmeier C, Barres BA, Tessier-Lavigne M. 1996. Hepatocyte growth factor/scatter factor is an axonal chemoattractant and a neurotrophic factor for spinal motor neurons. Neuron 17:1157–1172.

Glaser J, Gonzalez R, Perreau VM, Cotman CW, Keirstead HS. 2004. Neutralization of the chemokine CXCL10 enhances tissue sparing and angiogenesis following spinal cord injury. J Neurosci Res 77:701–708.

Grill R, Murai K, Blesch A, Gage FH, Tuszynski MH. 1997. Cellular delivery of neurotrophin-3 promotes corticospinal axonal growth and partial functional recovery after spinal cord injury. J Neurosci 17:5560–5572.

Guizar-Sahagun G, Ibarra A, Espitia A, Martinez A, Madrazo I, Franco-Bourland RE. 2005. Glutathione monoethyl ester improves functional recovery, enhances neuron survival, and stabilizes spinal cord blood flow after spinal cord injury in rats. Neuroscience 130:639–649.

Hagg T, Oudega M. 2006. Degenerative and spontaneous regenerative processes after spinal cord injury. J Neurotrauma 23:264–280.

Hamanoue M, Takemoto N, Matsumoto K, Nakamura T, Nakajima K, Kohsaka S. 1996. Neurotrophic effect of hepatocyte growth factor on central nervous system neurons in vitro. J Neurosci Res 43:554–564.

Hayashi K, Morishita R, Nakagami H, Yoshimura S, Hara A, Matsumoto K, Nakamura T, Ogihara T, Kaneda Y, Sakai N. 2001. Gene therapy for preventing neuronal death using hepatocyte growth factor: in vivo gene transfer of HGF to subarachnoid space prevents delayed neuronal death in gerbil hippocampal CA1 neurons. Gene Ther 8:1167–1173.

Hisahara S, Yuan J, Momoi T, Okano H, Miura M. 2001. Caspase-11 mediates oligodendrocyte cell death and pathogenesis of autoimmune-mediated demyelination. J Exp Med 193:111–122.

Igawa T, Matsumoto K, Kanda S, Saito Y, Nakamura T. 1993. Hepatocyte growth factor may function as a renotropic factor for regeneration in rats with acute renal injury. Am J Physiol 265:F61–F69.

Ikegami T, Nakamura M, Yamane J, Katoh H, Okada S, Iwanami A, Watanabe K, Ishii K, Kato F, Fujita H, Takahashi T, Okano HJ, Toyama Y, Okano H. 2005. Chondroitinase ABC combined with neural stem/progenitor cell transplantation enhances graft cell migration and outgrowth of growth-associated protein-43-positive fibers after rat spinal cord injury. Eur J Neurosci 22:3036–3046.

Jakeman LB, Wei P, Guan Z, Stokes BT. 1998. Brain-derived neurotrophic factor stimulates hindlimb stepping and sprouting of cholinergic fibers after spinal cord injury. Exp Neurol 154:170–184.

Kaneko S, Iwanami A, Nakamura M, Kishino A, Kikuchi K, Shibata S, Okano HJ, Ikegami T, Moriya A, Konishi O, Nakayama C, Kumagai K, Kimura T, Sato Y, Goshima Y, Taniguchi M, Ito M, He Z, Toyama Y, Okano H. 2006. A selective Sema3A inhibitor enhances regenerative responses and functional recovery of the injured spinal cord. Nat Med 12:1380–1389.

Kim JE, Liu BP, Park JH, Strittmatter SM. 2004. Nogo-66 receptor prevents raphespinal and rubrospinal axon regeneration and limits functional recovery from spinal cord injury. Neuron 44:439–451.

Kobayashi NR, Fan DP, Giehl KM, Bedard AM, Wiegand SJ, Tetzlaff W. 1997. BDNF and NT-4/5 prevent atrophy of rat rubrospinal neurons after cervical axotomy, stimulate GAP-43 and Talpha1-tubulin mRNA expression, and promote axonal regeneration. J Neurosci 17:9583–9595.

Kono S, Nagaike M, Matsumoto K, Nakamura T. 1992. Marked induction of hepatocyte growth factor mRNA in intact kidney and spleen in response to injury of distant organs. Biochem Biophys Res Commun 186:991–998.

Lilley CE, Groutsi F, Han Z, Palmer JA, Anderson PN, Latchman DS, Coffin RS. 2001. Multiple immediate-early gene-deficient herpes simplex virus vectors allowing efficient gene delivery to neurons in culture and widespread gene delivery to the central nervous system in vivo. J Virol 75:4343–4356.

Liu Y, Kim D, Himes BT, Chow SY, Schallert T, Murray M, Tessler A, Fischer I. 1999. Transplants of fibroblasts genetically modified to express BDNF promote regeneration of adult rat rubrospinal axons and recovery of forelimb function. J Neurosci 19:4370–4387.

Loy DN, Crawford CH, Darnall JB, Burke DA, Onifer SM, Whittemore SR. 2002. Temporal progression of angiogenesis and basal lamina deposition after contusive spinal cord injury in the adult rat. J Comp Neurol 445:308–324.

Maina F, Klein R. 1999. Hepatocyte growth factor, a versatile signal for developing neurons. Nat Neurosci 2:213–217.

Matsumoto K, Nakamura T. 1997. Hepatocyte growth factor (HGF) as a tissue organizer for organogenesis and regeneration. Biochem Biophys Res Commun 239:639–644.

Mautes AE, Weinzierl MR, Donovan F, Noble LJ. 2000. Vascular events after spinal cord injury: contribution to secondary pathogenesis. Phys Ther 80:673–687.

McTigue DM, Horner PJ, Stokes BT, Gage FH. 1998. Neurotrophin-3 and brain-derived neurotrophic factor induce oligodendrocyte proliferation and myelination of regenerating axons in the contused adult rat spinal cord. J Neurosci 18:5354–5365.

Miyazawa T, Matsumoto K, Ohmichi H, Katoh H, Yamashima T, Nakamura T. 1998. Protection of hippocampal neurons from ischemia-induced delayed neuronal death by hepatocyte growth factor: a novel neurotrophic factor. J Cereb Blood Flow Metab 18:345–348.

Morishita R, Aoki M, Hashiya N, Yamasaki K, Kurinami H, Shimizu S, Makino H, Takesya Y, Azuma J, Ogihara T. 2004. Therapeutic angiogenesis using hepatocyte growth factor (HGF). Curr Gene Ther 4:199–206.

Nagayama T, Nagayama M, Kohara S, Kamiguchi H, Shibuya M, Katoh Y, Itoh J, Shinohara Y. 2004. Post-ischemic delayed expression of hepatocyte growth factor and c-Met in mouse brain following focal cerebral ischemia. Brain Res 999:155–166.

Nakamura T, Nawa K, Ichihara A. 1984. Partial purification and characterization of hepatocyte growth factor from serum of hepatectomized rats. Biochem Biophy Res Commun 122:1450–1459.

Nakamura T, Nishizawa T, Hagiya M, Seki T, Shimonishi M, Sugimura A, Tashiro K, Shimizu S. 1989. Molecular cloning and expression of human hepatocyte growth factor. Nature 342:440–443.

Nakamura Y, Morishita R, Higaki J, Kida I, Aoki M, Moriguchi A, Yamada K, Hayashi S, Yo Y, Matsumoto K, et al. 1995. Expression of local hepatocyte growth factor system in vascular tissues. Biochem Biophys Res Commun 215:483–488.

Nakamura Y, Morishita R, Nakamura S, Aoki M, Moriguchi A, Matsumoto K, Nakamura T, Higaki J, Ogihara T. 1996. A vascular modulator, hepatocyte growth factor, is associated with systolic pressure. Hypertension 28:409–413.

Niimura M, Takagi N, Takagi K, Mizutani R, Ishihara N, Matsumoto K, Funakoshi H, Nakamura T, Takeo S. 2006. Prevention of apoptosis-inducing factor translocation is a possible mechanism for protective effects of hepatocyte growth factor against neuronal cell death in the hippocampus after transient forebrain ischemia. J Cereb Blood Flow Metab (in press).

Noji S, Tashiro K, Koyama E, Nohno T, Ohyama K, Taniguchi S, Nakamura T. 1990. Expression of hepatocyte growth factor gene in endothelial and Kupffer cells of damaged rat livers, as revealed by in situ hybridization. Biochem Biophys Res Commun 173:42–47.

Okura Y, Arimoto H, Tanuma N, Matsumoto K, Nakamura T, Yamashima T, Miyazawa T, Matsumoto Y. 1999. Analysis of neurotrophic effects of hepatocyte growth factor in the adult hypoglossal nerve axotomy model. Eur J Neurosci 11:4139–4144.

Palmer JA, Branston RH, Lilley CE, Robinson MJ, Groutsi F, Smith J, Latchman DS, Coffin RS. 2000. Development and optimization of herpes simplex virus vectors for multiple long-term gene delivery to the peripheral nervous system. J Virol 74:5604–5618.

Ramon-Cueto A, Plant GW, Avila J, Bunge MB. 1998. Long-distance axonal regeneration in the transected adult rat spinal cord is promoted by olfactory ensheathing glia transplants. J Neurosci 18:3803–3815.

Saruhashi Y, Young W, Perkins R. 1996. The recovery of 5-HT immunoreactivity in lumbosacral spinal cord and locomotor function after thoracic hemisection. Exp Neurol 139:203–213.

Shimamura M, Sato N, Oshima K, Aoki M, Kurinami H, Waguri S, Uchiyama Y, Ogihara T, Kaneda Y, Morishita R. 2004. Novel therapeutic strategy to treat brain ischemia: overexpression of hepatocyte growth factor gene reduced ischemic injury without cerebral edema in rat model. Circulation 109:424–431.

Shimamura M, Sato N, Waguri S, Uchiyama Y, Hayashi T, Iida H, Nakamura T, Ogihara T, Kaneda Y, Morishita R. 2006. Gene transfer of hepatocyte growth factor gene improves learning and memory in the chronic stage of cerebral infarction. Hypertension 47:742–751.

Sun W, Funakoshi H, Matsumoto K, Nakamura T. 2000. A sensitive quantification method for evaluating the level of hepatocyte growth factor and c-met/HGF receptor mRNAs in the nervous system using competitive RT-PCR. Brain Res Brain Res Protoc 5:190–197.

Tamura M, Nakamura M, Ogawa Y, Toyama Y, Miura M, Okano H. 2005. Targeted expression of anti-apoptotic protein p35 in oligodendrocytes reduces delayed demyelination and functional impairment after spinal cord injury. Glia 51:312–321.

Tuszynski MH, Peterson DA, Ray J, Baird A, Nakahara Y, Gage FH. 1994. Fibroblasts genetically modified to produce nerve growth factor induce robust neuritic ingrowth after grafting to the spinal cord. Exp Neurol 126:1–14.

Tuszynski MH, Gabriel K, Gage FH, Suhr S, Meyer S, Rosetti A. 1996. Nerve growth factor delivery by gene transfer induces differential outgrowth of sensory, motor, and noradrenergic neurites after adult spinal cord injury. Exp Neurol 137:157–173.

Vavrek R, Girgis J, Tetzlaff W, Hiebert GW, Fouad K. 2006. BDNF promotes connections of corticospinal neurons onto spared descending interneurons in spinal cord injured rats. Brain 129:1534–1545.

Wong V, Glass DJ, Arriaga R, Yancopoulos GD, Lindsay RM, Conn G. 1997. Hepatocyte growth factor promotes motor neuron survival and synergizes with ciliary neurotrophic factor. J Biol Chem 272:5187–5191.

Yamagata T, Muroya K, Mukasa T, Igarashi H, Momoi M, Tsukahara T, Arahata K, Kumagai H, Momoi T. 1995. Hepatocyte growth factor specifically expressed in microglia activated Ras in the neurons, similar to the action of neurotrophic factors. Biochem Biophys Res Commun 210:231–237.

Yanagita K, Matsumoto K, Sekiguchi K, Ishibashi H, Niho Y, Nakamura T. 1993. Hepatocyte growth factor may act as a pulmotrophic factor on lung regeneration after acute lung injury. J Biol Chem 268:21212–21217.

Zhao MZ, Nonoguchi N, Ikeda N, Watanabe T, Furutama D, Miyazawa D, Funakoshi H, Kajimoto Y, Nakamura T, Dezawa M, Shibata MA, Otsuki Y, Coffin RS, Liu WD, Kuroiwa T, Miyatake S. 2006. Novel therapeutic strategy for stroke in rats by bone marrow stromal cells and ex vivo HGF gene transfer with HSV-1 vector. J Cereb Blood Flow Metab 26:1176–1188.

Development/Plasticity/Repair

In Vivo Tracing of Neural Tracts in the Intact and Injured Spinal Cord of Marmosets by Diffusion Tensor Tractography

Kanehiro Fujiyoshi,[1,2]* Masayuki Yamada,[4,5]* Masaya Nakamura,[1] Junichi Yamane,[1,2] Hiroyuki Katoh,[1] Kazuya Kitamura,[1,2] Kenji Kawai,[4] Seiji Okada,[6] Suketaka Momoshima,[3] Yoshiaki Toyama,[1] and Hideyuki Okano[2]

Department of [1]Orthopaedic Surgery, [2]Physiology, and [3]Radiology and [4]Center for Integrated of Medical Research, Keio University School of Medicine, Shinjuku, Tokyo 160-8582, Japan, [5]Central Institute for Experimental Animals, Miyamae-ku, Kawasaki, Kanagawa 216-0001, Japan, and [6]Department of Research Superstar Program Stem Cell Unit, Graduate School of Medical Science, Kyushu University, Fukuoka 812-8582, Japan

In spinal cord injury, axonal disruption results in motor and sensory function impairment. The evaluation of axonal fibers is essential to assess the severity of injury and efficacy of any treatment protocol, but conventional methods such as tracer injection in brain parenchyma are highly invasive and require histological evaluation, precluding clinical applications. Previous advances in magnetic resonance imaging technology have led to the development of diffusion tensor tractography (DTT) as a potential modality to perform *in vivo* tracing of axonal fibers. The properties and clinical applications of DTT in the brain have been reported, but technical difficulties have limited DTT studies of the spinal cord. In this study, we report the effective use of DTT to visualize both intact and surgically disrupted spinal long tracts in adult common marmosets. To verify the feasibility of spinal cord DTT, we first performed DTT of postmortem marmosets. DTT clearly illustrated spinal projections such as the corticospinal tract and afferent fibers in control animals, and depicted the severed long tracts in the injured animals. Histology of the spinal cords in both control and injured groups were consistent with DTT findings, verifying the accuracy of DTT. We also conducted DTT in live marmosets and demonstrated that DTT can be performed in live animals to reveal *in vivo* nerve fiber tracing images, providing an essential tool to evaluate axonal conditions in the injured spinal cord. Taken together, these findings demonstrate the feasibility of applying DTT to preclinical and clinical studies of spinal cord injury.

Key words: **spinal cord injury; corticospinal tract; diffusion tensor tractography; magnetic resonance imaging; common marmoset; calmodulin-dependent protein kinase II-α; pathway-specific DTT; *in vivo* tracing**

Introduction

We established previously a reproducible spinal cord injury (SCI) model in adult common marmosets and demonstrated that transplantation of human neural stem/progenitor cells into the injured spinal cord promoted functional recovery (Iwanami et al., 2005b). An increase of axonal fibers, evaluated through histological methods, was observed near the transplanted neural stem/progenitor cells and were interpreted to be involved in the functional improvement. Such evaluation of axonal fibers is essential to assess the severity of SCI and efficacy of any treatment protocol (Olson, 2002; Kaneko et al., 2007), but conventional methods such as tracer injection in brain parenchyma are technically demanding and highly invasive (Ralston and Ralston, 1985; Lacroix et al., 2004). Because histological examinations are required to evaluate tracer studies, it has been impossible to evaluate axonal fibers *in vivo* and follow the sequential growth of axonal fibers in the same animal. Understanding the value of such an examination method, we therefore sought to establish a noninvasive method to evaluate axonal fibers *in vivo*.

Magnetic resonance imaging (MRI) is essential for predicting prognosis and planning the treatment of patients with SCI (Kulkarni et al., 1987; Yamashita et al., 1990). Our previous study using common marmosets also demonstrated that MRI could detect pathological changes after SCI (Iwanami et al., 2005a). However, the information provided by conventional T1- and T2-weighted MRI of the spinal cord is essentially limited to the differentiation of the white matter from the gray matter. Conventional MRI depicts the white matter as a uniform tissue, although it actually contains a complex array of directionally oriented nerve fibers. Methods to visualize the pathways of the white matter *in vivo* have been long sought and, recently, diffusion tensor tractography (DTT) has demonstrated this ability (Ito et al., 2002; Masutani et al., 2003; Mori et al., 2003).

Diffusion tensor imaging (DTI) is a new imaging technique that takes advantage of the anisotropic nature of water diffusion in biological tissue to obtain detailed microstructural information (Le Bihan et al., 1986; Moseley et al., 1990; Basser et al., 1994; Beaulieu, 2002; Mori and Zhang, 2006). By analyzing and reconstructing that data obtained by DTI, DTT can follow the orienta-

Received July 24, 2007; accepted Sept. 4, 2007.

This work was supported by grants from the Leading Project for Realization of Regenerative Medicine from the Ministry of Education, Culture, Sports, Science and Technology (MEXT) of Japan, from the Japan Science and Technology Corporation, from the General Insurance Association, and by a grant-in-aid from the 21st Century COE Program of MEXT, Japan, to Keio University. We thank Hirotaka James Okano and Ichio Aoki for critical review of this manuscript, Humika Toyoda for tender animal care, and Ai Yokokawa for technical assistance.

*K.F. and M.Y. contributed equally to this work.

The authors declare no competing financial interests.

Correspondence should be addressed to Hideyuki Okano, 35 Shinanomachi, Shinjuku-ku, Tokyo 160-8582, Japan. E-mail: hidokano@sc.itc.keio.ac.jp.

DOI:10.1523/JNEUROSCI.3354-07.2007

 0270-6474/07/2711991-08$15.00/0

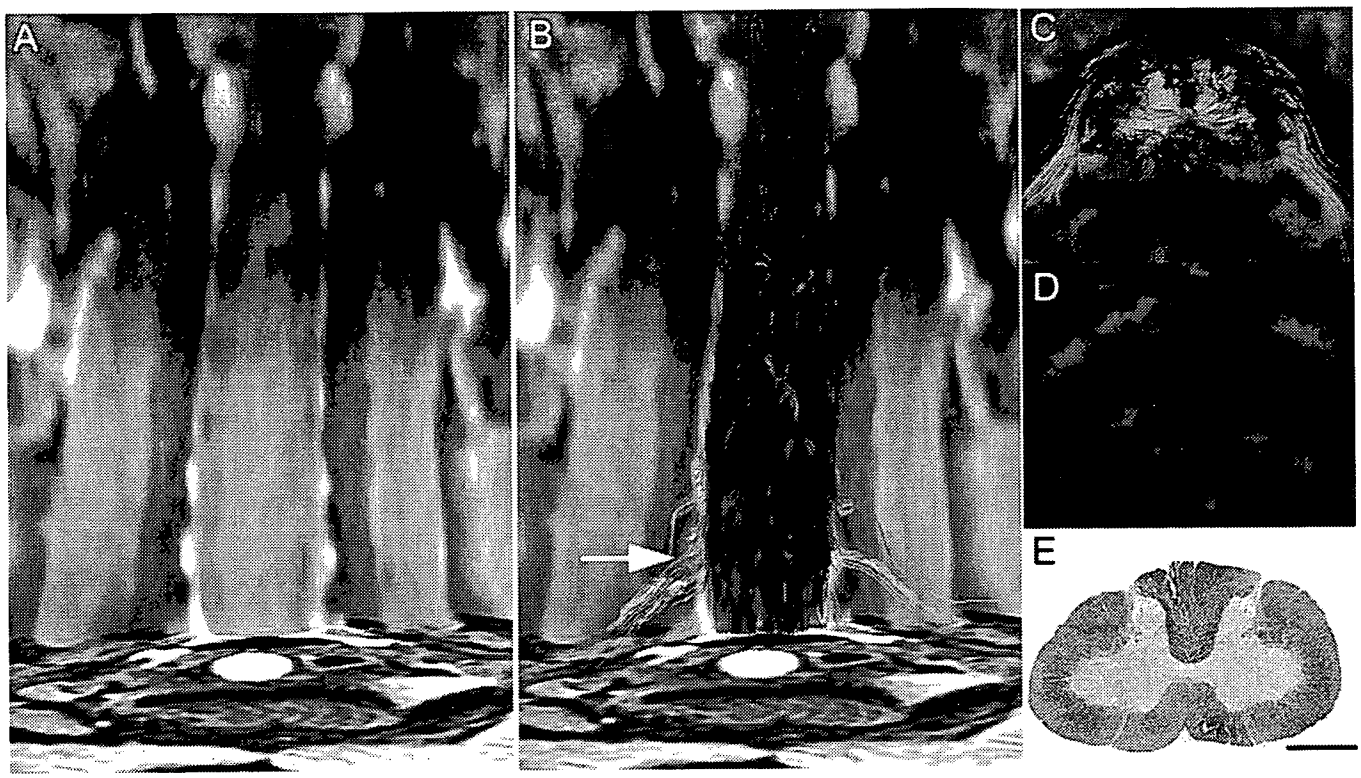

Figure 1. DTT of the intact spinal cord in a postmortem common marmoset. ***A***, Coronal T2-weighted MRI. ***B***, ***C***, Full-width DTT of the spinal cord (***B***) and an axial section (***C***) superimposed on axial T2-weighted images. The ROI was placed in the lower cervical spinal cord and DTT was traced in the cranial direction. DTT tracts are color coded to indicate tract orientation: red for left–right orientation, green for anterior–posterior orientation, and blue for superior–inferior orientation. ***D***, ***E***, Directionally color-coded axial FA map of the spinal cord (***D***) reveals that the configuration of the white matter depicted in blue is consistent with the myelin-positive area in an axial section of the same area stained with LFB (***E***). ***C–E*** are axial images of the C5/6 level (***B***, arrow). Scale bar, 1 mm.

tion of nerve fibers to trace specific neural pathways such as the corticospinal tract (CST) in the brain (Conturo et al., 1999; Masutani et al., 2003; Kamada et al., 2005a; Lee et al., 2005). Compared with the brain, however, DTT of the spinal cord is more difficult because of its smaller size and *in vivo* bulk motion (Basser and Jones, 2002; Maier and Mamata, 2005; Kharbanda et al., 2006). Several researchers have reported previously on successful DTT of the human spinal cord (Holder et al., 2000; Facon et al., 2005; Tsuchiya et al., 2005; Ducreux et al., 2006). However, because these DTT images were not confirmed with detailed histological studies, whether DTT actually reflects the anatomical axonal fibers remains unclear. In this study, we performed DTT of both intact and injured spinal cords in common marmosets and confirmed the accuracy of DTT through histology.

Materials and Methods

Hemisection SCI in common marmoset. Adult female common marmosets (266–384 g; Clea Japan, Tokyo, Japan) were used in the present study ($n = 6$). All interventions and animal care procedures were performed in accordance with the Laboratory Animal Welfare Act, the *Guide for the Care and Use of Laboratory Animals* (National Institutes of Health), and the *Guidelines and Policies for Animal Surgery* provided by the Animal Study Committee of the Central Institute for Experimental Animals of Keio University, and were approved by the ethics committee of Keio University. All surgeries were performed under general anesthesia induced by intramuscular injection of ketamine (50 mg/kg; Sankyo, Tokyo, Japan) and xylazine (5 mg/kg; Bayer, Leverkusen, Germany) and maintained by isoflurane (Foren; Abbott, Tokyo, Japan). The animal's pulse, arterial oxygen saturation, and rectal temperature were monitored during the surgical procedures. After a laminectomy at the C6 level, the dura mater was opened longitudinally and the right side of the spinal cord was cut at the C6 level using a surgical scalpel in the hemisection group ($n = 3$). The control group in this study in was a naive control without any surgical intervention.

Magnetic resonance imaging. MRI was performed using a 7.0 tesla MRI, PharmaScan 70/16 (BioSpin; Bruker) with a coil dedicated for small animals. In the studies using postmortem animals (control and hemisection groups, $n = 2$ each), conventional T2-weighted images (T2WIs) were first obtained, followed by intracardiac perfusion with 4% paraformaldehyde (PFA), pH 7.4, and diffusion tensor MRI. T2WI and diffusion tensor MRI of the hemisected animals were conducted 2 weeks after injury. DTI data sets were acquired with a spin-echo sequence based on the Stejskal–Tanner diffusion preparation. Scanning parameters were as follows: repetition time (TR), 15000 ms; echo time (TE), 40 ms; flip angle, 90°, field of view (FOV), 55 × 55 mm; acquisition data matrix, 256 × 256; reconstructed image resolution, 0.215 mm (with zero-filling interpolation); slice thickness, 0.85 mm; b-value, 1000 s/mm^2; motion-probing gradient (MPG) orientations, 12 axes; number of averaging (NA), 1. In the studies using live animals (control and hemisection group, $n = 1$ each), conventional and diffusion tensor MRI were performed under the general anesthesia as mentioned above. MRI scans of the hemisected animal were conducted 2 weeks after injury. In live animals, to reduce motion artifacts from the blood flow and CSF flow, animals were immobilized on an acrylic bed with a specially designed head positioner and electrocardiogram (ECG) probe (SA Instruments) for gated imaging was attached to the animal's front thorax. DTI data sets in live animals were acquired with an ECG-gated standard diffusion weighted spin-echo pulse sequence based on the Stejskal–Tanner diffusion preparation (Stejskal and Tanner, 1965). Scanning parameters were as follows: TR, 3500 ms; TE, 40 ms; flip angle, 90°; FOV, 40 × 40 mm; acquisition data matrix, 128 × 128; reconstructed image resolution, 0.31 × 0.31 mm; slice thickness, 0.94 mm; b-value, 1000 s/mm^2; MPG orientations, 12 axes; NA, 1.

Diffusion tensor analysis. Diffusion tensor and three-dimensional analysis were performed using Volume One and dTVIISR software (Kuni-

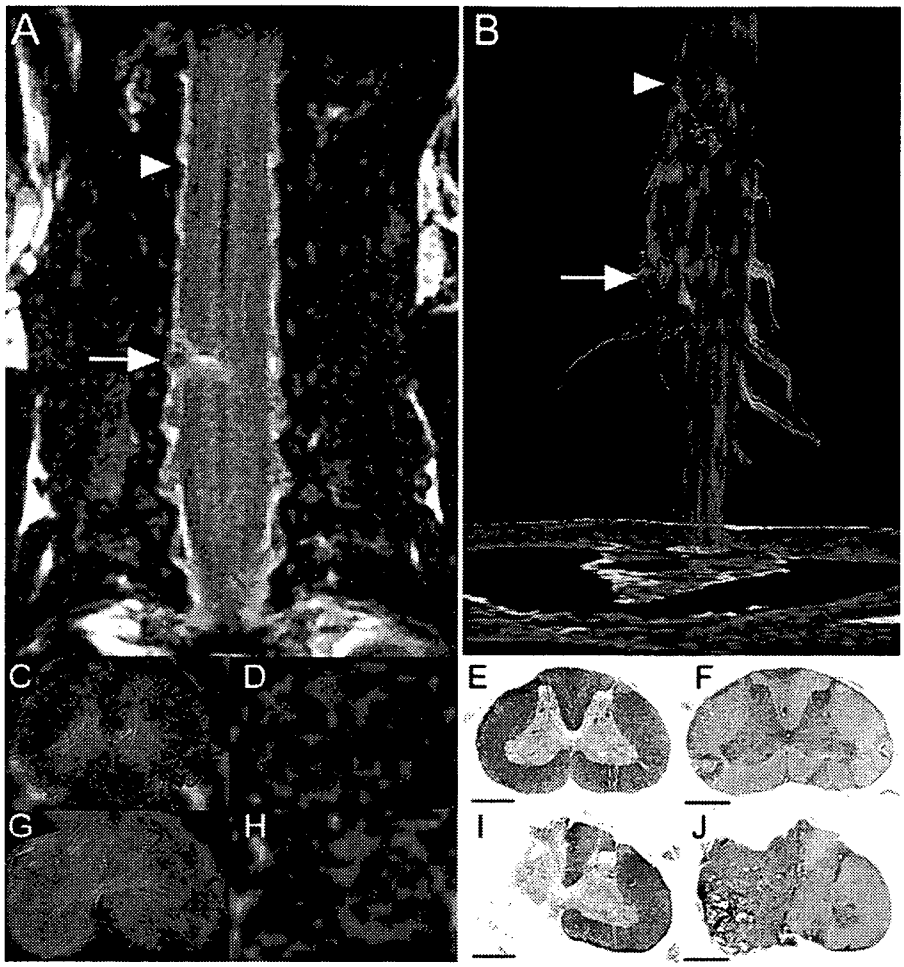

Figure 2. DTT of the hemisected spinal cord at 2 weeks after injury in a postmortem common marmoset. ***A***, Coronal T2-weighted MRI depicted the hemisection injury as a low-intensity area with no change in the cord caudal to the injury. ***B***, DTT of the hemisected spinal cord. The ROI was placed in the upper cervical spinal cord, and DTT was traced in the caudal direction revealing disruption of white matter fibers on the hemisected side. The traced tracts became untraceable at the injury site, whereas tracts on the contralateral side continued caudally. Arrows indicated the hemisection site and arrowheads indicated the point 8 mm cranial to the injury site in ***A*** and ***B***. ***C–J***, DTT (***C***, ***G***), FA map (***D***, ***H***), LFB staining (***E***, ***I***), and HE staining (***F***, ***J***) of the spinal cord 8 mm cranial to the injury site (***C–F***) and at the hemisection site (***G–J***). Although normal FA and anatomy of the spinal cord was confirmed cranial to the hemisection site, there was a significant decrease in FA of the white matter fibers at the hemisection site (***G***, ***H***). Consistent with these changes in DTT (***G***) and color-coded FA map (***H***), demyelination was seen at the hemisection site (***I***). Scale bars, 1 mm.

matsu et al., 2003; Masutani et al., 2003). An eigenvector ($e1$) associated with the largest eigenvalue ($\lambda 1$) was assumed to represent the local fiber direction. Fiber tracking was initiated from a manually selected region of interest (ROI) area, which is the "seed" from which tracking lines were propagated bidirectionally according to the eigenvector ($e1$) at each voxel pixel. The direction of diffusion anisotropy was followed until tracking was terminated when it reached a voxel with a fractional anisotropy of <0.25. To delineate the motor tracts, the seed was placed on the area histologically known to contain CaMKII-α-positive fibers in the upper cervical cord, which corresponds to the CST (Terashima et al., 1994; Iwanami et al., 2005a). To delineate the afferent pathways of the spinal cord, we placed the seed at the anterolateral and posterior funiculi of the lower cervical cord, which correspond to the spinothalamic tract and the gracile fasciculus, respectively. We used the two-regions-of-interest method (Mori et al., 2003), which consists of seed and target regions to depict the pyramidal decussation from the medullary pyramid (seed) to the opposite CST area in the upper cervical cord (target).

Histological analyses. In the postmortem group, spinal cord tissues were removed after diffusion tensor MRI. In the live group, each animal was perfused intracardially with 4% paraformaldehyde after diffusion tensor MRI and then the spinal cord tissues were removed. All spinal cord specimens were postfixed in 4% PFA and immersed overnight in 10% sucrose followed by 30% sucrose. Frozen section blocks were prepared and cut into 20-μm-thick axial sections using a cryostat. These sections were stained with hematoxylin-eosin (HE) for general histological examinations and Luxol fast blue (LFB) for evaluation of the myelinated area. Immunostaining with anti-CaMKII-α antibody (primary antibody, diluted 1:100, mouse monoclonal; Zymed, San Francisco, CA; secondary antibody, a biotin-labeled goat anti-mouse IgG for ABC and DAB staining) was performed to examine the CST.

Results

DTT of intact and injured spinal cords in postmortem common marmosets

Based on the data from *in vivo* high-resolution diffusion tensor MR images of postmortem common marmoset spinal cords (Fig. 1*A*), we created a DTT of the cervical spinal cord that enabled us to detect various fibers of the spinal cord (Fig. 1*B*). In a color-coded DTT of the intact cervical spinal cord, each path traced by DTT, which we will refer to have as a tract, is depicted in colors according to its orientation (Pajevic and Pierpaoli, 1999): red for left–right orientation, green for anterior–posterior orientation, and blue for superior–inferior orientation (Fig. 1*B*,*C*). White matter fibers with high craniocaudal diffusion anisotropy were visible in blue on color-coded maps of fractional anisotropy (FA) (Basser and Pierpaoli, 1996), an index of anisotropy ranging from 0 (perfectly isotropic diffusion) to 1 (a hypothetical infinite cylinder), which had been calculated from the same data (Fig. 1*D*) and the distribution of longitudinal fibers was consistent with the distribution of myelinated axons stained with LFB (Fig. 1*E*). In the gray matter, horizontal fibers passing from the central canal to the anterior horn of the spinal cord were observed in red, but almost no diffusion anisotropy was detected in the remaining gray matter, which is mainly occupied by neuronal and glial cells.

In the marmosets with hemisected spinal cords, the hemisected area of spinal cord appeared as a high-intensity area in coronal T2WIs 2 weeks after injury (Fig. 2*A*). DTT of the hemisected spinal cord revealed that the longitudinal fibers of the white matter in the injured side were disrupted at the hemisection site, but preserved in the intact side (Fig. 2*B*). In axial DTT images and color-coded FA maps, there was a significant decrease in FA of the longitudinal fibers of the white matter as well as the transverse fibers of the gray matter at the hemisection site (Fig. 2*G*,*H*), compared with the site 8 mm cranial to the hemisection site (Fig. 2*C*,*D*). Consistent with these changes in DTT and colored FA maps, histology of the hemisected area revealed disruption of both gray and white matter with severe demyelination. (Fig. 2*I*,*J*).

Pathway-specific DTT in postmortem common marmosets

To examine the feasibility of visualizing individual pathways in common marmosets, we analyzed the CST from the medulla to the upper cervical spinal cord because the course of the CST in this region is unique and well known. Analysis of histological sections stained for calmodulin-dependent protein kinase II-α (CaMKII-α) determined the location of the CST (Terashima et al., 1994; Iwanami et al., 2005a) within the medulla, and DTT of the CST was performed by setting the ROI, which is a manually selected area based on anatomical knowledge from which DTT fiber tracking was initiated, in the pyramid of the medulla and tracing caudally (Fig. 3*A*). The course of the CST in this area has been well documented in the literature; the majority of fibers cross to the contralateral side through the pyramidal decussation and descended the lateral funiculus (lateral CST), whereas a small group of fibers descend the ipsilateral anterior (anterior CST) and lateral funiculus (anterolateral CST) (Qiu et al., 1991; Lacroix et al., 2004; Lemon et al., 2004). A study in humans demonstrated the composition of the CST, with the lateral CST accounting for 90% of CST fibers and the anterior CST and uncrossed lateral CST accounting for the remaining 8 and 2%, respectively (Carpenter and Sutin, 1983). DTT was capable of tracing fibers through all three courses and successfully demonstrated the pyramidal decussation of the CST (Fig. 3*B–E*). However the number of tracts depicted with DTT through each course did not reflect the amount of CST fibers traveling through each pathway, because the number of DTT tracts depicted descending each pathway were similar although a majority of CST fibers actually travel through the lateral CST.

We focused on the pyramidal decussation of the CST and conducted histological studies to verify the results of DTT. DTT and histological sections from similar points along the craniocaudal axis were compared. The course of the CST depicted by DTT (Fig. 3*H*) corresponded to the area positive for CaMKII-α (Fig. 3*I*), which recognizes fibers of the CST, and LFB staining of the same section (Fig. 3*J*) confirmed that the CST delineated by DTT and CaMKII-α contained myelinated fibers. CST-specific DTT superimposed on MR images verified that the pyramidal decussation was depicted in the proper position (Fig. 3*F*,*G*).

With sufficient data to indicate that CST-specific DTT is possible, we then con-

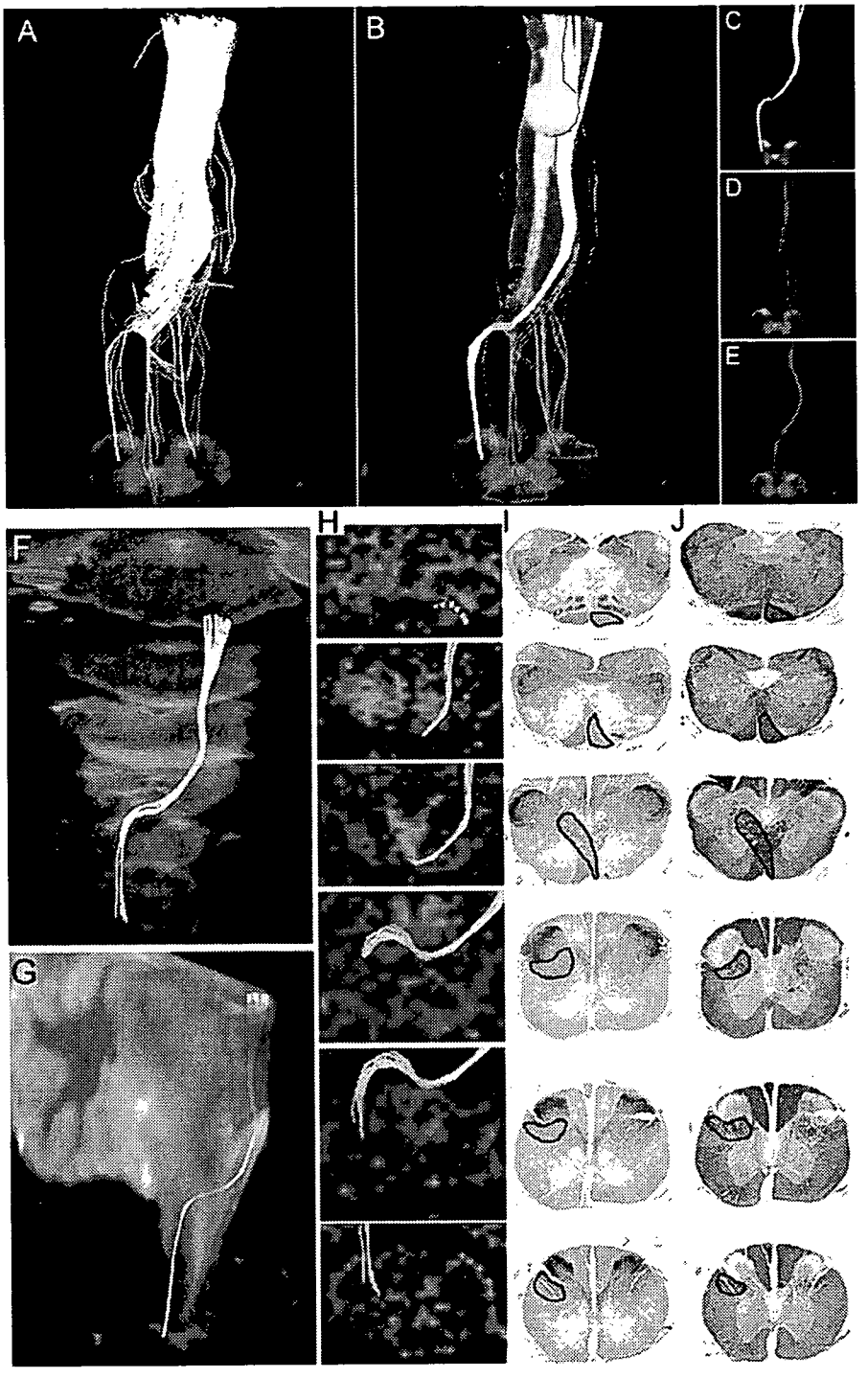

Figure 3. Pathway-specific DTT in a postmortem common marmoset revealing the course of the corticospinal tract with pyramidal decussation. ***A***, DTT of the CST was conducted by placing the ROI in the pyramid of the medulla and tracing caudally. Note that the volume of traced tracts decrease as the tracing was carried caudally, because many tracts became untraceable because of the partial volume effect. ***B***, By placing secondary ROIs in areas of the upper cervical spinal cord known to contain CST fibers, CST fibers that pass through both ROIs could be depicted. ***C***, Lateral CST fibers that crossed over to and descended the contralateral lateral funiculus in a pattern suggesting pyramidal decussation were depicted in yellow. ***D***, Uncrossed lateral fibers descending the ipsilateral lateral funiculus were depicted in red. ***E***, Lateral fibers descending the ipsilateral anterior funiculus were depicted in blue. The fact that DTT was capable of accurately depicting all three known pathways of the CST is significant. However, it is important to note that the depicted DTT tracts do not accurately reflect the volume of nerve fibers, because it is known that the lateral CST contains the majority of CST fibers. ***F***, ***G***, DTT of the pyramidal decussation superimposed on three-dimensional MR images to macroscopically confirm that the pyramidal decussation was depicted in the proper height in the medulla and the upper cervical cord, using the cerebellum as a reference point. ***H***, DTT of the pyramidal decussation superimposed on axial color-coded FA maps. ***I***, ***J***, Axial histological slices of the same points in ***H*** stained for CaMKII-α to reveal the location of CST fibers (***I***) and LFB to delineate the configuration of the white matter (***J***). In each slice, the area through which the DTT CST tract passes was positive for CaMKII-α and LFB, confirming the accuracy of DTT.

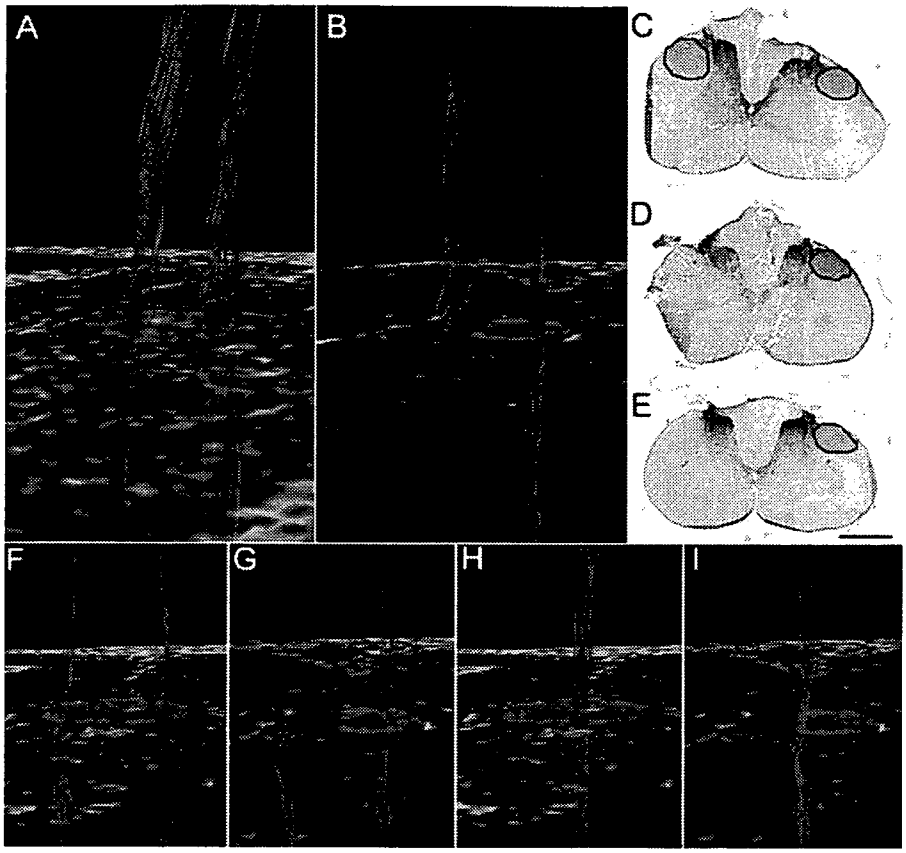

Figure 4. *In vivo* CST- and afferent pathway-specific DTT of intact and injured spinal cords in postmortem common marmosets. ***A***, DTT of an intact CST superimposed on a color-coded FA map of the C5/6 level. ***B***, DTT of the CST in a hemisected spinal cord superimposed on a color-coded FA map of the hemisected C5/6 level 2 weeks after injury revealing disruption of the CST at the site of injury. ***C–E***, CaMKII-α staining of an axial section of the hemisected spinal cord 8 mm cranial to the hemisection site (***C***), at the hemisection site (***D***), and 8 mm caudal to the hemisection site (***E***). Because CaMKII-α is a known substance transported in the axons of the CST, the absence of CaMKII-α staining distal to the injury suggested CST disruption, confirming the results of CST-specific DTT. ***F***, ***H***, In the control group, ROI was placed at the anterolateral funiculus (***F***) or the posterior funiculus (***H***), and a DTT of the afferent pathways was drawn in the caudocranial direction. ***G***, ***I***, In the hemisection group, no fibers were observed at the site rostral to the hemisection site, demonstrating that tract-specific DTT can potentially delineate the spinothalamic tract (***G***) and dorsal column-medial lemniscus pathway (***I***). Scale bar, 1 mm.

ducted CST-specific DTT of hemisected spinal cords to observe how DTT would depict an injured pathway. CST-specific DTTs of the middle to lower cervical spinal cord were compared in intact and hemisected postmortem common marmosets. In the intact cervical spinal cord, DTT depicted descending CST tracts in the bilateral lateral funiculus (Fig. 4*D*). In the hemisected cervical spinal cord 2 weeks after injury, FA decreased in color-coded FA maps and no tracts were found caudal to the hemisection site on the injured side whereas the intact CST pathway was observed descending the uninjured side (Fig. 4*B*). Histology confirmed the disruption of the CST at the hemisection site with robust CaMKII-α staining rostral to the hemisection (Fig. 4*C*) and no CaMKII-α positive CST fibers at and caudal to the hemisection site (Fig. 4*D*,*E*).

Using a similar technique, it is also possible to trace pathways other than the CST. By placing the ROI in areas known to contain afferent fibers and tracing in the caudocranial direction, the spinothalamic tract in the anterolateral funiculus (Fig. 4*F*) and the medial lemniscus pathway in the posterior funiculus (Fig. 4*B*) were depicted. When the same procedure was repeated in the hemisected group, the ascending tracts were disrupted at the hemisection site with no tracts rostral to the lesion on the injured side, whereas normal ascending tracts were observed in the uninjured side (Fig. 4*G*,*I*).

Pathway-specific DTT of intact and injured spinal cords in live common marmosets

To evaluate the clinical feasibility of DTT, we repeatedly performed *in vivo* pathway-specific DTT on live animals and compared the results with those obtained from postmortem animals. Similar to the DTT of postmortem animals, *in vivo* DTT of the intact cervical CST in live animals showed longitudinal tracts in the lateral funiculus bilaterally (Fig. 5*B*), and pathway-specific DTT of afferent fibers depicted tracts in the anterolateral and posterior funiculus (Figs. 5*C*,*D*). In the hemisected marmoset 2 weeks after injury, T2WI MRI revealed a low-intensity area at the hemisection site and a high-intensity area at the same level on the intact side (Fig. 5*E*), whereas DTT showed disruption of the CST (Fig. 5*F*) and ascending fibers at the lesion site (Fig. 5*G*,*H*). Pathway-specific *in vivo* DTT findings in live animals were highly similar to those of postmortem animals, especially in major tract morphology. Because MRI scans of live animals required anesthesia, the scan duration and, therefore, scan area were considerably limited compared with postmortem animals; MRIs of live animals were conducted in 1.5 h whereas 10 h scans were performed for postmortem animals. Overall, these findings demonstrated that it is feasible to depict the descending and ascending pathways of the spinal cord in live animals using pathway-specific DTT, and demonstrate the usefulness of DTT as an imaging method to assess specific pathways in spinal cord injuries.

Discussion

Because we hope to clinically apply this procedure to human SCI patients in the future, common marmosets were selected for this study. As primates, they are closely related to humans in terms of neurofunctional anatomy of the spinal cord. For example, the CST fibers localize mainly in the dorsal funiculus in rodents, whereas in primates they are mainly located in the lateral funiculus (Qiu et al., 1991; Terashima et al., 1994; Lacroix et al., 2004; Lemon et al., 2004; Iwanami et al., 2005a). From a practical standpoint, common marmosets are easy to handle, breed effectively, and are small enough to fit into the narrow MRI coil.

In our past studies of SCI in common marmosets, we have used contusion injury models because, compared with other SCI methods, contusion injuries more closely resemble the pathological conditions found in human SCI patients (Iwanami et al., 2005a,b). In this study, however, we chose a hemisection model because the disruption and regeneration of axons after a hemisection injury is easier to evaluate than a contusion injury (Levi et al., 2002; Tuszynski et al., 2002). Because the main objective of this study was to evaluate the usefulness of DTT in assessing axonal

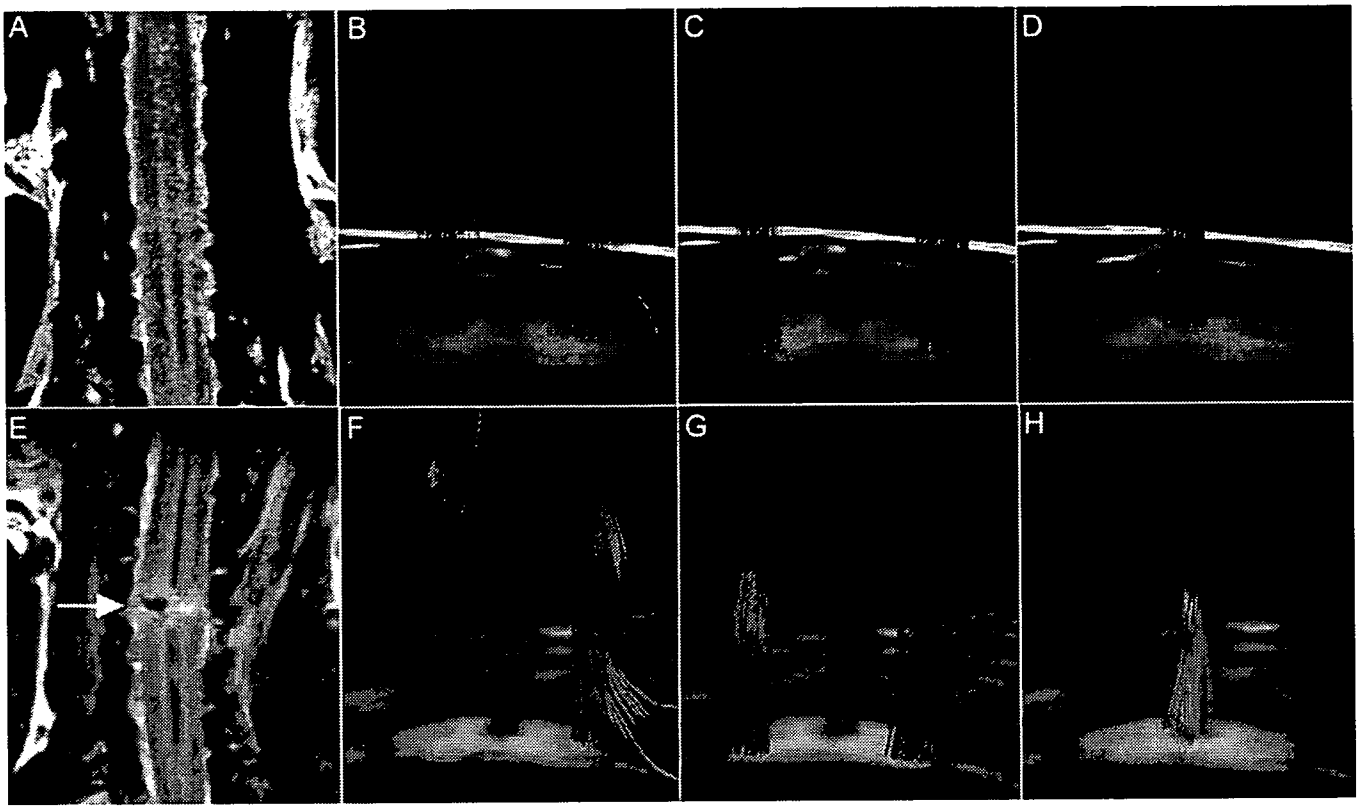

Figure 5. ***A–H***, *In vivo* pathway-specific DTT of intact and injured spinal cords in live common marmosets. MRI and tract-specific DTT of the intact spinal cord (***A–D***) and hemisected spinal cord 2 weeks after injury (***E–H***). DTTs of the CST (***B***, ***F***), spinothalamic tract (***C***, ***G***), and dorsal column-medial lemniscus pathway (***D***, ***H***) were conducted in both groups, revealing tract disruption at the hemisection site (C5/6 level) in all pathways. Although there are some limitations, pathway-specific *in vivo* DTT conducted in live animals yielded results similar to those observed in postmortem animals, especially in respect to major tract morphology.

conditions in SCI and to confirm the accuracy of DTT by comparing DTT images with histological findings, an injury with less complexity and ambiguousness was desired. With the convincing images obtained in this study, it would be interesting to examine contusion injury models in the future.

With the ability to visualize axonal projections in three-dimensions, DTT has tremendous potential as a tool to diagnose and evaluate CNS disease and trauma. In fact, DTT is already being clinically applied to visualize cerebral long tracts in cerebral surgery (Kamada et al., 2005b; Okada et al., 2006). Although there have been several preliminary studies of spinal cord DTI and DTT, they have not fully explored the potential of DTI technology. One reason DTI of the spinal cord has been less studied compared with the brain is the technical difficulty involved in conducting imaging of the spinal cord. DTI of the spinal cord requires high spatial resolution, is easily affected by magnetic susceptibility, and is obscured by *in vivo* bulk motion brought about by the beating of the heart, respiration, and the flow of CSF (Basser and Jones, 2002; Maier and Mamata, 2005; Kharbanda et al., 2006). In the present study, a 7.0 tesla MRI was used to obtain images with high resolution and a spin echo protocol was used to minimize magnetic susceptibility. To eliminate the effect of *in vivo* bulk motion, we first conducted our study using postmortem animals. Because a previous study demonstrated a degradation of diffusion anisotropy in the postmortem spinal cord (Matsuzawa et al., 1995; Madi et al., 2005), we performed all imaging immediately after animals were killed. By using postmortem animals it was possible to conduct scans of long duration (an average scan time of 10 h), resulting in images with high spatial resolution.

In our study using live animals, all animals were maintained under general anesthesia and cardiac-gated imaging was incorporated to minimize the effects of bulk motion. Under general anesthesia, marmosets were immobilized on an acrylic bed with a specially designed head positioner. Because the total scan duration was limited by anesthetic considerations, scan time (average 1.5 h) and, therefore, scan area and spatial resolution were limited compared with postmortem animal studies. However, it is of enormous importance that DTT of a live animal was able to visualize intact neural pathways and also the disrupted pathways in an injured animal, because this is the only method currently available or in development that can reveal *in vivo* axonal pathways.

In this study, we focused mainly on the CST to conduct pathway-specific DTT because it is the most important pathway in terms of motor function and often becomes the subject of scrutiny in studies of spinal cord injury treatment protocols. CST-specific DTT accurately depicted the course of the CST from the medulla to the cervical spinal cord and succeeded in imaging the "pyramidal decussation," which has been considered difficult to visualize. Furthermore, CST-specific DTT of the hemisected animal revealed the disruption of the CST at the site of injury. By using the dTV DTT software (Kunimatsu et al., 2003; Masutani et al., 2003), it is also possible to set the ROI at any point of interest and to perform voxel unit fiber tracking from that position within the threshold limit set for diffusion anisotropy. This allowed us to conduct DTT of the afferent pathways in both intact and injured spinal cords, illustrating the enormous value of this method. This capability to visualize specific projections can be applied to various studies of the spinal cord. For example, an

interesting study would be a study of ascending projections and its involvement in allodynia, using functional MRI to assess sensory dysfunction (Hofstetter et al., 2005; Lilja et al., 2006).

DTT is a new technique that traces white matter fiber trajectories by tracking the direction of faster diffusion, which is assumed to correspond to the longitudinal axis of the tract. However it is important to keep in mind that the tracking is conducted in units called voxels, which, in this study, is 0.215 mm in size, considerably larger than any one individual axonal tract. Therefore, what is actually being tracked is a group of axonal fibers with perhaps some tissue other than the intended fibers at times included in the same voxel (Mori and van Zijl, 2002; Mori and Zhang, 2006). When tissues other than the targeted axonal tract are present within the same voxel, their diffusion anisotropy interferes destructively in a phenomenon referred to as partial volume effect (Alexander et al., 2001). For example, if multiple axonal fiber tracts with different trajectories cross within the same voxel, their diffusion anisotropy becomes merged and may become more isotropic, losing directional information. The tracking procedure is often terminated because the path comes to a voxel that has lost directional orientation (anisotropy) as a result of this partial volume effect (Fig. 3*A–E*). Partial volume effect can also result in a misleading redirection of anisotropy, leading to incorrect fiber tracking. It is also important to understand that the number of tracts traced by DTT does not necessarily reflect the actual volume of white matter fiber trajectories (Fig. 3*A–E*).

With the convincing images obtained in this study, the possibilities and the limitations of spinal cord DTT need to be further explored. For example, the next step would be DTT of contusion SCI models. Another significant point that needs to be studied, is whether DTT has the sensitivity to detect regenerating axons. If confirmed, DTT would allow tracing studies at multiple time points in the same animal/patient, becoming an indispensable tool to monitor and evaluate the effectiveness of any treatment protocol for spinal cord injury. Whatever the results reveal, DTT of the spinal cord is a powerful tool with tremendous potential if its properties and limitations are fully understood and correctly applied.

References

Alexander AL, Hasan KM, Lazar M, Tsuruda JS, Parker DL (2001) Analysis of partial volume effects in diffusion-tensor MRI. Magn Reson Med 45:770–780.

Basser PJ, Jones DK (2002) Diffusion-tensor MRI: theory, experimental design and data analysis—a technical review. NMR Biomed 15:456–467.

Basser PJ, Pierpaoli C (1996) Microstructural and physiological features of tissues elucidated by quantitative-diffusion-tensor MRI. J Magn Reson B 111:209–219.

Basser PJ, Mattiello J, LeBihan D (1994) MR diffusion tensor spectroscopy and imaging. Biophys J 66:259–267.

Beaulieu C (2002) The basis of anisotropic water diffusion in the nervous system—a technical review. NMR Biomed 15:435–455.

Carpenter MB, Sutin J (1983) Human neuroanatomy, Ed 8, pp 282–289. Baltimore: Lippincott, Williams and Wilkins.

Conturo TE, Lori NF, Cull TS, Akbudak E, Snyder AZ, Shimony JS, McKinstry RC, Burton H, Raichle ME (1999) Tracking neuronal fiber pathways in the living human brain. Proc Natl Acad Sci USA 96:10422–10427.

Ducreux D, Lepeintre JF, Fillard P, Loureiro C, Tadie M, Lasjaunias P (2006) MR diffusion tensor imaging and fiber tracking in 5 spinal cord astrocytomas. AJNR Am J Neuroradiol 27:214–216.

Facon D, Ozanne A, Fillard P, Lepeintre JF, Tournoux-Facon C, Ducreux D (2005) MR diffusion tensor imaging and fiber tracking in spinal cord compression. AJNR Am J Neuroradiol 26:1587–1594.

Hofstetter CP, Holmstrom NA, Lilja JA, Schweinhardt P, Hao J, Spenger C, Wiesenfeld-Hallin Z, Kurpad SN, Frisen J, Olson L (2005) Allodynia limits the usefulness of intraspinal neural stem cell grafts; directed differentiation improves outcome. Nat Neurosci 8:346–353.

Holder CA, Muthupillai R, Mukundan Jr S, Eastwood JD, Hudgins PA (2000) Diffusion-weighted MR imaging of the normal human spinal cord *in vivo*. AJNR Am J Neuroradiol 21:1799–1806.

Ito R, Mori S, Melhem ER (2002) Diffusion tensor brain imaging and tractography. Neuroimaging Clin N Am 12:1–19.

Iwanami A, Yamane J, Katoh H, Nakamura M, Momoshima S, Ishii H, Tanioka Y, Tamaoki N, Nomura T, Toyama Y, Okano H (2005a) Establishment of graded spinal cord injury model in a nonhuman primate: the common marmoset. J Neurosci Res 80:172–181.

Iwanami A, Kaneko S, Nakamura M, Kanemura Y, Mori H, Kobayashi S, Yamasaki M, Momoshima S, Ishii H, Ando K, Tanioka Y, Tamaoki N, Nomura T, Toyama Y, Okano H (2005b) Transplantation of human neural stem cells for spinal cord injury in primates. J Neurosci Res 80:182–190.

Kamada K, Todo T, Morita A, Masutani Y, Aoki S, Ino K, Kawai K, Kirino T (2005a) Functional monitoring for visual pathway using real-time visual evoked potentials and optic-radiation tractography. Neurosurgery 57 [Suppl]:121–127.

Kamada K, Todo T, Masutani Y, Aoki S, Ino K, Takano T, Kirino T, Kawahara N, Morita A (2005b) Combined use of tractography-integrated functional neuronavigation and direct fiber stimulation. J Neurosurg 102:664–672.

Kaneko S, Iwanami A, Nakamura M, Kishino A, Kikuchi K, Shibata S, Okano HJ, Ikegami T, Moriya A, Konishi O, Nakayama C, Kumagai K, Kimura T, Sato Y, Goshima Y, Taniguchi M, Ito M, He Z, Toyama Y, Okano H (2007) A selective Sema3A inhibitor enhances regenerative responses and functional recovery of the injured spinal cord. Nat Med 12:1380–1389.

Kharbanda HS, Alsop DC, Anderson AW, Filardo G, Hackney DB (2006) Effects of cord motion on diffusion imaging of the spinal cord. Magn Reson Med 56:334–339.

Kulkarni MV, Williams JC, Yeakley JW, Andrews JL, McArdle CB, Narayana PA, Howell RR, Jonas AJ (1987) Magnetic resonance imaging in the diagnosis of the cranio-cervical manifestations of the mucopolysaccharidoses. Magn Reson Imaging 5:317–323.

Kunimatsu A, Aoki S, Masutani Y, Abe O, Mori H, Ohtomo K (2003) Three-dimensional white matter tractography by diffusion tensor imaging in ischaemic stroke involving the corticospinal tract. Neuroradiology 45:532–535.

Lacroix S, Havton LA, McKay H, Yang H, Brant A, Roberts J, Tuszynski MH (2004) Bilateral corticospinal projections arise from each motor cortex in the macaque monkey: a quantitative study. J Comp Neurol 473:147–161.

Le Bihan D, Breton E, Lallemand D, Grenier P, Cabanis E, Laval-Jeantet M (1986) MR imaging of intravoxel incoherent motions: application to diffusion and perfusion in neurologic disorders. Radiology 161:401–407.

Lee JS, Han MK, Kim SH, Kwon OK, Kim JH (2005) Fiber tracking by diffusion tensor imaging in corticospinal tract stroke: topographical correlation with clinical symptoms. NeuroImage 26:771–776.

Lemon RN, Kirkwood PA, Maier MA, Nakajima K, Nathan P (2004) Direct and indirect pathways for corticospinal control of upper limb motoneurons in the primate. Prog Brain Res 143:263–279.

Levi AD, Dancausse H, Li X, Duncan S, Horkey L, Oliviera M (2002) Peripheral nerve grafts promoting central nervous system regeneration after spinal cord injury in the primate. J Neurosurg 96:197–205.

Lilja J, Endo T, Hofstetter C, Westman E, Young J, Olson L, Spenger C (2006) Blood oxygenation level-dependent visualization of synaptic relay stations of sensory pathways along the neuroaxis in response to graded sensory stimulation of a limb. J Neurosci 26:6330–6336.

Madi S, Hasan KM, Narayana PA (2005) Diffusion tensor imaging of *in vivo* and excised rat spinal cord at 7 T with an icosahedral encoding scheme. Magn Reson Med 53:118–125.

Maier SE, Mamata H (2005) Diffusion tensor imaging of the spinal cord. Ann NY Acad Sci 1064:50–60.

Masutani Y, Aoki S, Abe O, Hayashi N, Otomo K (2003) MR diffusion tensor imaging: recent advance and new techniques for diffusion tensor visualization. Eur J Radiol 46:53–66.

Matsuzawa H, Kwee IL, Nakada T (1995) Magnetic resonance axonography of the rat spinal cord: postmortem effects. J Neurosurg 83:1023–1028.

Mori H, Masutani Y, Aoki S, Abe O, Hayashi N, Masumoto T, Yamada H, Yoshikawa T, Kunimatsu A, Ohtomo K, Kabasawa H (2003) [Simple visualization of the corticospinal pathway using tractography: one-ROI

and two-ROI methods]. Nippon Igaku Hoshasen Gakkai Zasshi 63:51–53.

Mori S, van Zijl PC (2002) Fiber tracking: principles and strategies—a technical review. NMR Biomed 15:468–480.

Mori S, Zhang J (2006) Principles of diffusion tensor imaging and its applications to basic neuroscience research. Neuron 51:527–539.

Moseley ME, Cohen Y, Kucharczyk J, Mintorovitch J, Asgari HS, Wendland MF, Tsuruda J, Norman D (1990) Diffusion-weighted MR imaging of anisotropic water diffusion in cat central nervous system. Radiology 176:439–445.

Okada T, Mikuni N, Miki Y, Kikuta K, Urayama S, Hanakawa T, Fushimi Y, Yamamoto A, Kanagaki M, Fukuyama H, Hashimoto N, Togashi K (2006) Corticospinal tract localization: integration of diffusion-tensor tractography at 3-T MR imaging with intraoperative white matter stimulation mapping—preliminary results. Radiology 240:849–857.

Olson L (2002) Med: clearing a path for nerve growth. Nature 416:589–590.

Pajevic S, Pierpaoli C (1999) Color schemes to represent the orientation of anisotropic tissues from diffusion tensor data: application to white matter fiber tract mapping in the human brain. Magn Reson Med 42:526–540.

Qiu Y, Wada Y, Otomo E, Tsukagoshi H (1991) Morphometric study of cervical anterior horn cells and pyramidal tracts in medulla oblongata and the spinal cord in patients with cerebrovascular diseases. J Neurol Sci 102:137–143.

Ralston DD, Ralston III HJ (1985) The terminations of corticospinal tract axons in the macaque monkey. J Comp Neurol 242:325–337.

Stejskal EO, Tanner JE (1965) Spin diffusion measurements: spin echoes in the presence of a time dependent field gradient. J Chem Phys 42:288–292.

Terashima T, Ochiishi T, Yamauchi T (1994) Immunohistochemical detection of calcium/calmodulin-dependent protein kinase II in the spinal cord of the rat and monkey with special reference to the corticospinal tract. J Comp Neurol 340:469–479.

Tsuchiya K, Fujikawa A, Suzuki Y (2005) Diffusion tractography of the cervical spinal cord by using parallel imaging. AJNR Am J Neuroradiol 26:398–400.

Tuszynski MH, Grill R, Jones LL, McKay HM, Blesch A (2002) Spontaneous and augmented growth of axons in the primate spinal cord: effects of local injury and nerve growth factor-secreting cell grafts. J Comp Neurol 449:88–101.

Yamashita Y, Takahashi M, Matsuno Y, Sakamoto Y, Oguni T, Sakae T, Yoshizumi K, Kim EE (1990) Chronic injuries of the spinal cord: assessment with MR imaging. Radiology 175:849–854.

PNAS
Proceedings of the National Academy of Sciences of the United States of America www.pnas.org

A carbohydrate-binding protein, Galectin-1, promotes proliferation of adult neural stem cells

Masanori Sakaguchi, Tetsuro Shingo, Takuya Shimazaki, Hirotaka James Okano, Mieko Shiwa, Satoru Ishibashi, Hideyuki Oguro, Mikiko Ninomiya, Toshihiko Kadoya, Hidenori Horie, Akira Shibuya, Hidehiro Mizusawa, Françoise Poirier, Hiromitsu Nakauchi, Kazunobu Sawamoto, and Hideyuki Okano

PNAS 2006;103;7112-7117; originally published online Apr 24, 2006;
doi:10.1073/pnas.0508793103

A carbohydrate-binding protein, Galectin-1, promotes proliferation of adult neural stem cells

Masanori Sakaguchi[a,b], Tetsuro Shingo[c], Takuya Shimazaki[a], Hirotaka James Okano[a], Mieko Shiwa[d], Satoru Ishibashi[e], Hideyuki Oguro[f], Mikiko Ninomiya[a,g,h], Toshihiko Kadoya[i], Hidenori Horie[j], Akira Shibuya[b], Hidehiro Mizusawa[e], Françoise Poirier[k], Hiromitsu Nakauchi[f], Kazunobu Sawamoto[a,h], and Hideyuki Okano[a,l]

[a]Department of Physiology and [h]Bridgestone Laboratory of Developmental and Regenerative Neurobiology, Keio University School of Medicine, Tokyo 160-8582, Japan; [b]Institute of Basic Medical Sciences, University of Tsukuba, Ibaraki 305-8575, Japan; [c]Department of Neurological Surgery, Okayama University Graduate School of Medicine and Dentistry, Okayama 700-8558, Japan; [d]Yokohama Laboratory, Ciphergen Biosystems KK, Kanagawa 204-0005, Japan; [e]Department of Neurology and Neurological Science, Graduate School of Medicine, Tokyo Medical and Dental University, Tokyo 113-8596, Japan; [f]Laboratory of Stem Cell Therapy, Center for Experimental Medicine, Institute of Medical Sciences, University of Tokyo, Tokyo 108-8639, Japan; [g]Department of Neurology, Saitama Medical School, Saitama 350-0495, Japan; [i]CMC R&D Laboratories, Pharmaceutical Division, Kirin Brewery, Gunma 370-0013, Japan; [j]Advanced Research Center for Biological Science, Waseda University, Tokyo 202-0021, Japan; and [k]Institut Jacques Monod, Unité Mixte de Recherche Centre National de la Recherche Scientifique 7592, Universities Paris 6 and Paris 7, Cedex 05 Paris, France

Edited by Fred H. Gage, The Salk Institute for Biological Studies, San Diego, CA and approved March 15, 2006 (received for review October 8, 2005)

In the subventricular zone of the adult mammalian forebrain, neural stem cells (NSCs) reside and proliferate to generate young neurons. We screened factors that promoted the proliferation of NSCs *in vitro* by a recently developed proteomics technique, the ProteinChip system. In this screen, we identified a soluble carbohydrate-binding protein, Galectin-1, as a candidate. We show herein that Galectin-1 is expressed in a subset of slowly dividing subventricular zone astrocytes, which includes the NSCs. Based on results from intraventricular infusion experiments and phenotypic analyses of knockout mice, we demonstrate that Galectin-1 is an endogenous factor that promotes the proliferation of NSCs in the adult brain.

lectin | mobilization | stem cell niche

Recently, neural stem cells (NSCs) residing in the adult CNS have been studied to elucidate the mechanisms of ongoing tissue maintenance (1) and to develop strategies for regenerating the damaged CNS (2, 3).

Two neurogenic regions have been identified in the forebrain (FB): the subventricular zone (SVZ) of the lateral ventricle (LV) (4–6) and the subgranular layer of the hippocampal dentate gyrus (7–9). NSCs in these regions can generate functional neurons in the adult brain (10–12). Clinically, soluble factors that regulate these progenitor cells may be useful for regenerating the damaged CNS (13). The identification of additional factors that promote the proliferation of stem cells will contribute to NSC biology and to the development of innovative strategies for brain repair.

The proliferation and differentiation of various adult stem cells are regulated by common soluble factors (14). OP9 is a cell line that has been used to screen for factors that support hematopoietic stem cells (HSCs) (15, 16). In the present study, we found that OP9 conditioned medium (CM) promoted neurosphere formation, by which the proliferation of NSCs can be monitored *in vitro* (17). Using the ProteinChip system (18), we identified Galectin-1 as one of the molecules responsible for this activity.

Galectin-1 is a soluble carbohydrate-binding protein (19, 20) that has been implicated in a variety of biological events (21, 22). Carbohydrates on the cell surface may be involved in the intercellular interactions of various stem cells, including NSCs (23–25) and HSCs (26). A recent report suggested that Galectin-1 promotes the proliferation of HSCs *in vitro* (27). However, its functions in NSCs remain unknown. Here, we report on the expression and function of Galectin-1 in the adult mammalian brain.

Results and Discussion

Galectin-1 Was Found in OP9CM. To examine how OP9 cells affect the proliferation of NSCs, we cultured neurosphere cells (17) with or without OP9CM. At a density of one cell per well, no neurospheres formed in cultures grown without OP9CM (Fig. 1*A*, Ctrl; $n = 800$ cells) (28). In contrast, at the same culture density, of the total cells grown with OP9CM ($n = 400$), 49 ($12.4 \pm 0.54\%$) initiated neurosphere formation (Fig. 1*A*, OP9). Interestingly, the CM from OP9 cells that were passaged repeatedly over 6 months (inactivated OP9, IA-OP9) did not support neurosphere formation (Fig. 1*A*, IA-OP9; $n > 800$).

To identify the OP9-derived molecules that enhanced neurosphere formation, we used an expression screen based on mass spectrometry (18) to detect molecules that were more abundant in OP9CM than in IA-OP9CM. A signal at ≈14.6 kDa showed a reproducible difference in peak height between the two CMs (Fig. 5, which is published as supporting information on the PNAS web site). This fraction was purified, concentrated, and separated by SDS/PAGE, and the band was cut from the gel and analyzed by tandem mass spectrometry (see *Materials and Methods*). We obtained two amino acid sequences (VRGEVASDAK and EDGTWGTEHR) that were identical to portions of the Galectin-1 protein ($n = 3$), suggesting that the 14.6-kDa peak was Galectin-1. Western blotting with a specific Ab showed that the OP9CM contained more Galectin-1 than did the IA-OP9CM ($n = 3$; $P < 0.01$).

Adding recombinant Galectin-1 protein (10 and 100 ng/ml) to the culture medium enhanced the formation of neurospheres cultured at 100 cells per well (Fig. 1*B*; $P < 0.01$, ANOVA). Galectin-1 did not mimic the full activity of the OP9CM, suggesting that there are other factors that enhance neurosphere formation in the OP9CM. The neurospheres grown with Galectin-1 (100 ng/ml) were larger (Fig. 6*A*, which is published as supporting information on the PNAS web site; $P < 0.05$), formed more secondary neurospheres (Fig. 6*B*; $P < 0.05$), and differentiated into neurons, astrocytes, and oligodendrocytes (Fig. 1*C*). Together, these results suggest that Galectin-1 is one of the factors in OP9CM that enhances neurosphere formation.

Expression of Galectin-1 in the Adult Mouse FB. To investigate the *in vivo* function of Galectin-1, we examined its expression in the

Conflict of interest statement: No conflicts declared.

This paper was submitted directly (Track II) to the PNAS office.

Freely available online through the PNAS open access option.

Abbreviations: SVZ, subventricular zone; LV, lateral ventricle; FB, forebrain; GFAP, glial fibrillary acidic protein; PCNA, proliferating cell nuclear antigen; NSC, neural stem cell; CM, conditioned medium; IA-OP9, inactivated OP9.

[l]To whom correspondence should be addressed at: Department of Physiology, Keio University School of Medicine, 35 Shinano-machi, Shinjuku-ku, Tokyo 160-8582, Japan. E-mail: hidokano@sc.itc.keio.ac.jp.

www.pnas.org/cgi/doi/10.1073/pnas.0508793103

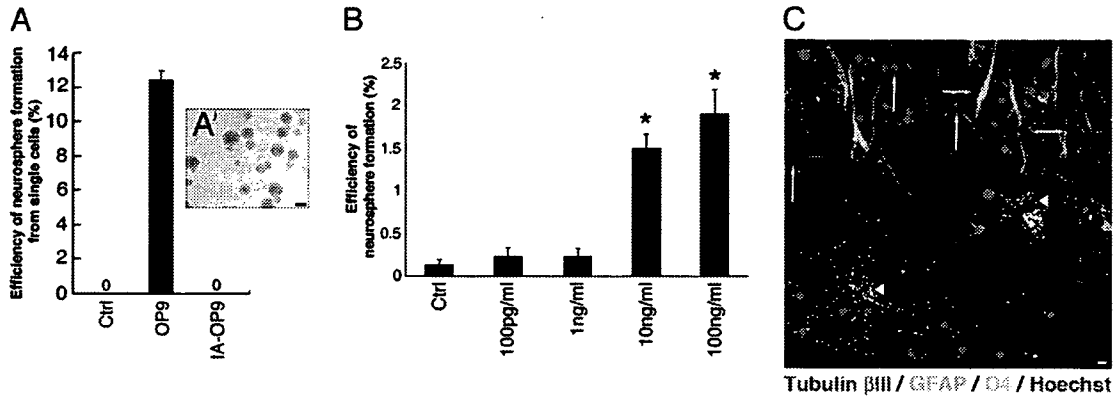

Fig. 1. Galectin-1 enhances neurosphere formation. (*A*) Effects of CM on neurosphere formation. Ctrl, control. (*A'*) The neurospheres initiated by OP9CM could be passaged more than five times. (*B*) Galectin-1 enhances neurosphere formation. Note that some neurospheres formed in the control cultures under this condition (culture density of 100 cells per well). *, $P < 0.01$. (*C*) The neurospheres initiated by Galectin-1 differentiated into neurons and glial cells. Representative images of differentiated cells from a neurosphere generated with recombinant Galectin-1 and immunostained with each neural lineage marker are shown. Tubulin βIII (neurons, red, white arrows), GFAP (astrocytes, green, green arrows), O4 (oligodendrocytes, light blue, arrowheads), and Hoechst (nucleus, dark blue) images were obtained by confocal laser microscopy. (Scale bars: *A*, 100 μm; *C*, 10 μm.)

mouse brain by using a Galectin-1-specific Ab (29). To confirm the specificity and sensitivity of the staining procedures, brain sections from a *galectin-1*-null mutant mouse (30) were simultaneously incubated with the same anti-Galectin-1 Ab, and we observed no staining (Fig. 7, which is published as supporting information on the PNAS web site).

In the adult mouse FB, as reported previously (31), subsets of neurons in the cortex were Galectin-1$^+$ (Fig. 7*A'*). In addition, we found Galectin-1 staining signals in the SVZ (Fig. 7*A''*) and dentate gyrus (Fig. 8*A*, which is published as supporting information on the PNAS web site), the two major adult neurogenic regions. RT-PCR analysis also showed that Galectin-1 is expressed in the SVZ (Fig. 8*B*). Almost all of the Galectin-1$^+$ cells in the adult SVZ expressed glial fibrillary acidic protein (GFAP) (Fig. 2*A*; see Fig. 8*C* for the confocal image), Nestin (Fig. 8*D*), and S100β (Fig. 8*E*). Some of these Galectin-1$^+$ cells were positive for Ki67 (Fig. 8*F*) (32), a nuclear marker of cellular replication. With regard to Galectin-1 expression in GFAP$^+$ cells outside the SVZ, we found that subsets of GFAP$^+$ cells in the subgranular layer and hilus were Galectin-1$^+$ (Fig. 8*A*), whereas most of the GFAP$^+$ cells in the cortex and striatum were Galectin-1$^-$ (Fig. 8 *G* and *H*). In the SVZ, the GFAP$^+$ astrocytes (type B cells) have been shown to act as NSCs (33, 34), which generate Dlx$^+$/Mash1$^+$ type C cells (35, 36) (Toida Kazunori, personal communication) and subsequently differentiate into PSA-NCAM$^+$/Dlx$^+$/Mash1$^-$ type A cells (in which PSA-NCAM is the polysialylated neural cell adhesion molecule) (35, 36). Among striatal neurons (Fig. 8*I*), Mash1$^+$ type C cells, and PSA-NCAM$^+$ type A cells (Fig. 8*J*), none showed Galectin-1 immunoreactivity. Dissociated SVZ cells were stained with

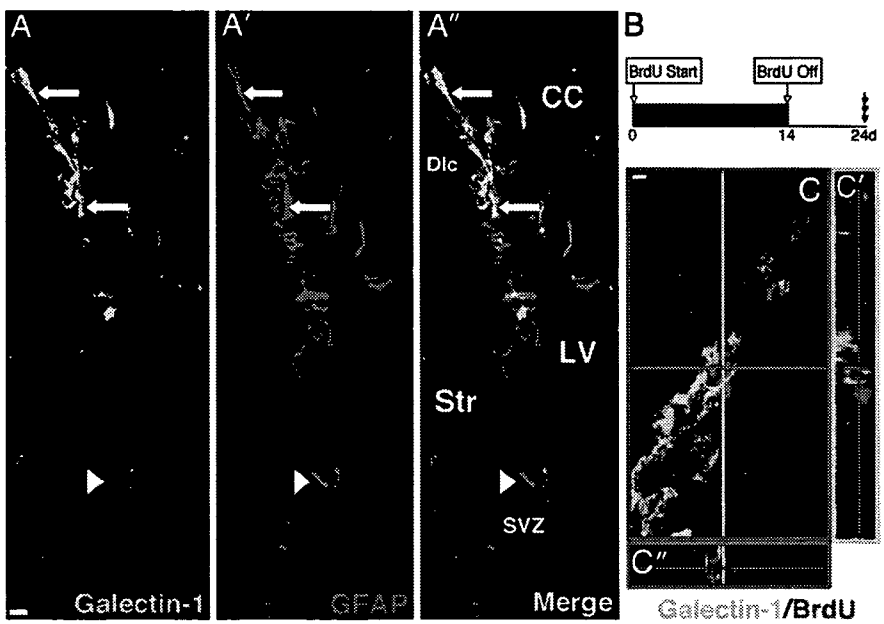

Fig. 2. Galectin-1 is detected in SVZ astrocytes. (*A*) Low-magnification images of Galectin-1 (*A*) and GFAP (*A'*) double immunostaining in the coronal section through the LV. Galectin-1 and GFAP double-positive cells are seen in the SVZ (arrows). Note there are some Galectin-1-negative cells among the GFAP$^+$ cells (e.g., arrowhead). (*A''*) Merged image. CC, corpus callosum; Str, striatum; Dlc, dorsolateral corner. (*B*) Experimental schema for marking slowly dividing cells. (*C*) Slowly dividing Galectin-1$^+$ cell. High-magnification confocal image of a Galectin-1 (green in cell soma) and BrdU (red in nucleus) double-positive cell in the SVZ. Sections were made after 2 weeks of oral BrdU administration followed by 10 days of wash-out. (*C'* and *C''*) 3D reconstruction images. (Scale bars: 5 μm.)

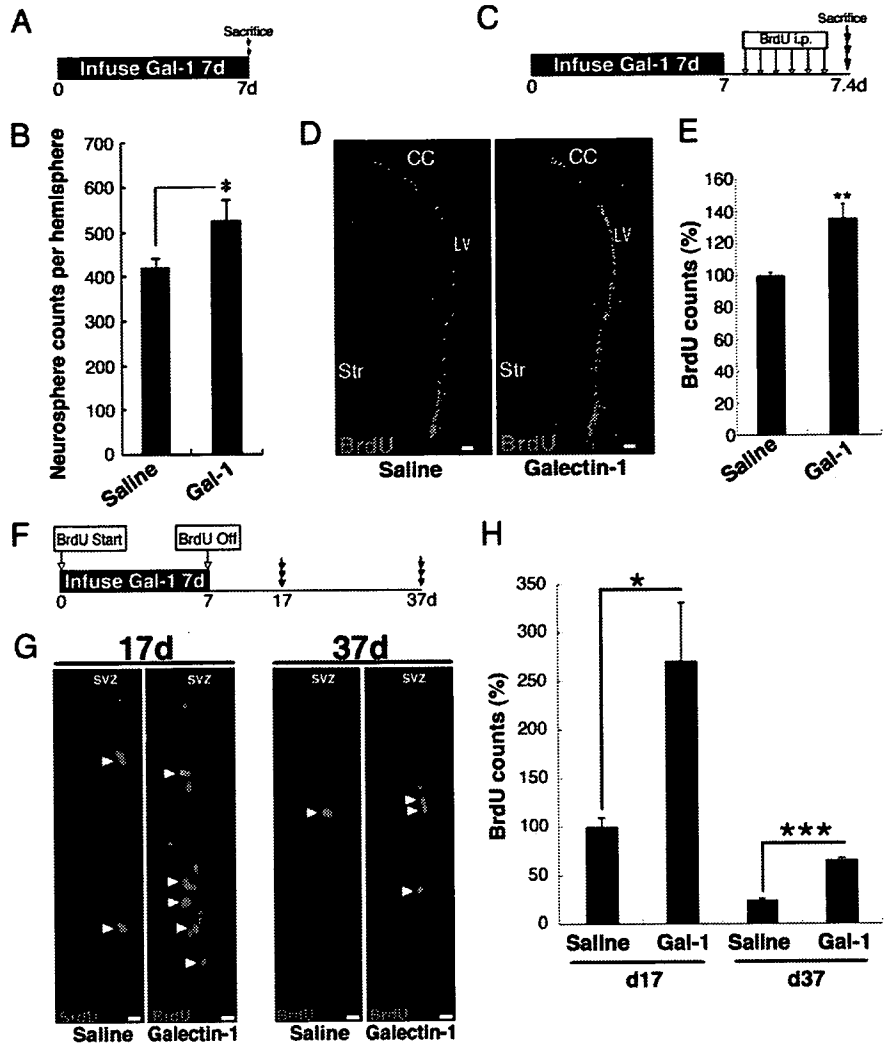

Fig. 3. Galectin-1 facilitates neural progenitor cell proliferation in the adult FB. (*A*) Experimental schema of the neurosphere formation assay after Galectin-1 infusion. (*B*) Galectin-1 significantly increased the number of neurosphere-initiating cells in the SVZ. *, $P < 0.05$. (*C*) Experimental schema of BrdU infusion after Galectin-1 infusion. (*D*) Low-magnification images of BrdU$^+$ cells in the SVZ after Galectin-1 infusion. (*E*) Galectin-1 infusion significantly increased the number of BrdU$^+$ cells in the SVZ. **, $P < 0.01$. (*F*) Experimental schema for labeling cells that retained BrdU long after Galectin-1 infusion. The mice were killed at the 17- or 37-day time point. (*G*) BrdU-labeled cells after infusion of saline or Galectin-1. (*H*) In the Galectin-1-infused brain, the number of BrdU$^+$ cells was significantly greater than in the saline-treated brain at 17 and 37 days. *, $P = 0.01$; ***, $P = 0.0006$. Str, striatum. (Scale bars: *D*, 50 μm; *G*, 15 μm.)

anti-Galectin-1 and anti-GFAP Abs to determine the percentages of each cell population in the SVZ. Of the total SVZ cells counted (n = 336 from three mice), 32.7 ± 6.38% (110 cells) were Galectin-1$^+$, and 31.3 ± 6.99% (105 cells) were GFAP$^+$. Of the GFAP$^+$ cells, 71.4 ± 1.48% were also Galectin-1$^+$. These results suggest that Galectin-1 is expressed in a subset of SVZ astrocytes.

To detect the slowly dividing NSC population in the SVZ (37), we gave BrdU to mice in their drinking water for 2 weeks and killed the mice 10 days later (Fig. 2*B*); this delay allowed the BrdU in the rapidly dividing type C cell population to be washed out and the type A cell population to migrate to a more rostral region, out of the SVZ (37). A subpopulation of the long-term BrdU-retaining cells expressed Galectin-1 (Fig. 2*C*). Thus, we conclude that Galectin-1 is expressed in a subset of GFAP$^+$ SVZ astrocytes that includes NSCs.

Galectin-1 Facilitates Proliferation of Neural Progenitor Cells in the Adult FB. The *in vitro* functions and *in vivo* expression pattern of Galectin-1 led us to examine whether it promotes adult neural progenitor proliferation *in vivo*. Galectin-1 protein was infused into the mouse LV for 7 days, and the number of neurospheres derived from the SVZ was counted (Fig. 3*A*); this number should reflect the number of progenitor cell types in the SVZ, including type B and C cells (36). As expected, significantly more neurospheres were formed by SVZ cells from the Galectin-1-infused adult brains than by SVZ cells from the control brains (Fig. 3*B*). The neurospheres in these cultures retained the properties of stem cells *in vitro*, and the proportion of neurons produced from the spheres was not significantly different (Galectin-1, 7.61 ± 0.61%; control, 5.84 ± 0.47%).

Next, we tested the effects of Galectin-1 on cell proliferation in the SVZ by infusing it into the LV, followed by BrdU injections every 2 h for 10 h (Fig. 3*C*). Thirty minutes after the last BrdU injection, the mice were killed. We counted the number of BrdU$^+$ cells in the SVZ of the LV and found a significant increase, on average, compared with the saline-infused control group (Fig. 3 *D* and *E*; $P < 0.01$; $n > 3$ mice each). There was no significant difference in the number of apoptotic cells in the SVZ between the two groups (Fig. 9 *A* and *B*, which is published as supporting information on the PNAS web site), suggesting that the Galectin-1-induced increase in BrdU$^+$ cells was caused by increased proliferation rather than increased cell survival.

Table 1. Galectin-1 increases the number of SVZ astrocytes in the adult brain

Treatment	No. of cells		
	Type B	Type C	Type A
Saline	40 ± 14	200 ± 12	64 ± 6.6
Galectin-1	66 ± 7.0*	280 ± 2.0*	64 ± 31
Galectin-1/saline relative ratio	1.7	1.4	1.0

Significantly increased numbers of SVZ astrocytes (type B cells) and type C cells were observed in the Galectin-1-infused brain. Data are the average counts from 50-μm sections. *, $P < 0.05$.

To determine what type of cells in the SVZ proliferated in response to the Galectin-1 infusion, we used cell-type markers (Fig. 10, which is published as supporting information on the PNAS web site) that allowed us to distinguish proliferating type B ($BrdU^+/Sox21^+/Dlx^-$), type C ($BrdU^+/Mash1^+$), and type A ($BrdU^+/Dlx^+/Mash1^-$) cells from others ($BrdU^+/Sox21^-$) (Table 1; see *Materials and Methods* for details). The Galectin-1 infusion significantly increased the number of proliferating type B and C cells (Table 1; $P < 0.05$, Mann–Whitney U test).

Infusion of Galectin-1 Protein Increases the Slowly Dividing SVZ Cells. We next examined the effect of Galectin-1 on the number of slowly dividing cells. We gave BrdU to mice in their drinking water during the 1-week infusion of Galectin-1 protein and killed them 17 or 37 days after the beginning of the infusion (Fig. 3*F*). There were significantly more $BrdU^+$ cells in the SVZ of the Galectin-1-infused brains than in that of the control brains at both time points (Fig. 3 *G* and *H*; day 17, $P = 0.01$, $n > 3$ each; day 37, $P < 0.001$, $n > 3$ each). These data suggest that Galectin-1 infusion increased the population of slowly dividing SVZ progenitor cells.

Galectin-1 exists in either a reduced or oxidized form, and only the reduced form possesses carbohydrate-binding activity (38). The infusion of CS-Galectin-1, a reduced form in which all of the cysteines responsible for its oxidation have been converted to serine (39), significantly increased the number of slowly dividing cells (Fig. 11, which is published as supporting information on the PNAS web site; day 17, $P < 0.001$, $n > 5$ mice each). In contrast, the oxidized Galectin-1 did not have a significant effect (Fig. 11*C*). These results suggest that the carbohydrate-binding capacity of the extracellularly administrated Galectin-1 is required for its effect on the number of slowly dividing cells. We also found that CS-Galectin-1 could bind to SVZ cells, including $GFAP^+$ astrocytes (unpublished data), suggesting that these cells are responsive to Galectin-1.

***Galectin-1*-Null Mice Have Fewer Neural Progenitor Cells in the Adult Brain.** To study the function of endogenous Galectin-1 in adult neural progenitor cells, we analyzed the phenotype of adult *galectin-1* mutant mice. First, we counted the number of cycling cells in the SVZ by using proliferating cell nuclear antigen (PCNA), a proliferation marker (40), and found significantly fewer in the *galectin-1*-null mice than in their wild-type littermates (Fig. 4 *A–C*; $P < 0.01$; $n > 3$ each). We also examined the number of type C cells by counting the $Mash1^+$ cells, of which there were also significantly fewer in the *galectin-1*-null mice than in wild-type littermates (Fig. 4 *D–F*; $P < 0.05$; $n > 3$ each). We then treated the animals with BrdU for 2 weeks, followed by a 10-day wash-out period (Fig. 4*G*), and found that there were significantly fewer slowly dividing cells in the SVZ of the *galectin-1*-null mice than in their wild-type littermates (Fig. 4 *H–J*; $P < 0.01$; $n > 3$ each). Furthermore, infusion of an

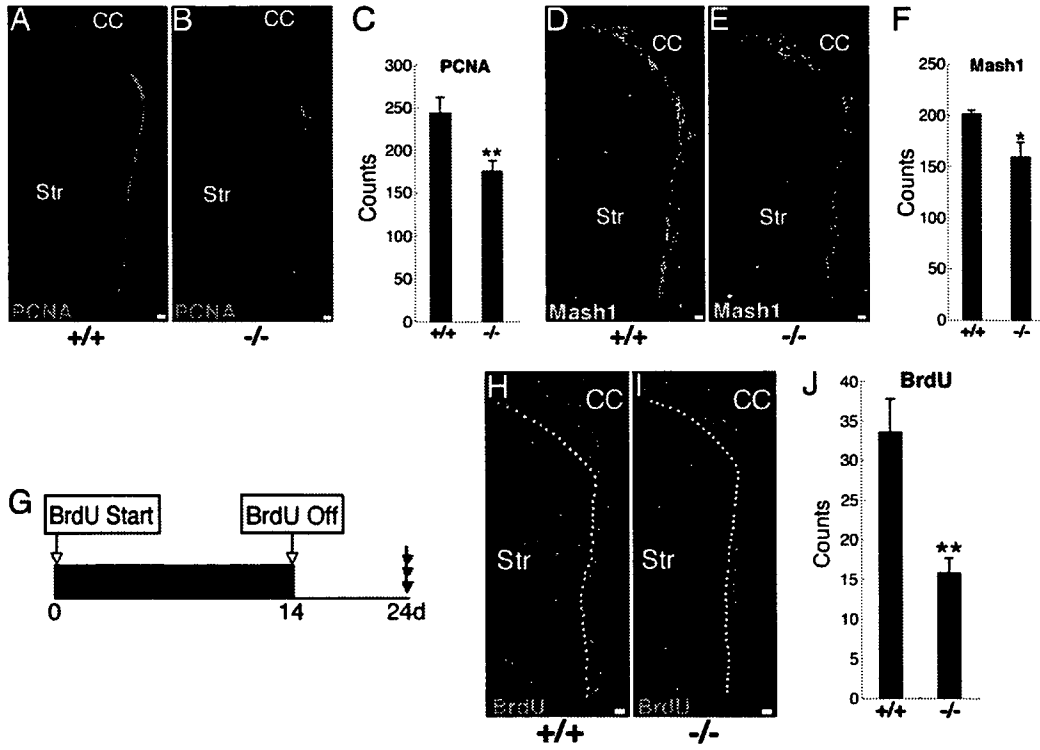

Fig. 4. Adult *galectin-1*-null mice show decreased neural progenitor cells. (*A–C*) Significantly fewer $PCNA^+$ cells were seen in the SVZ of *galectin-1*-null mice than in wild-type littermates. **, $P < 0.01$; $n > 3$ each. (*D–F*) Significantly fewer $Mash1^+$ type C cells were seen in the SVZ of *galectin-1* null mice than in wild-type littermates. *, $P < 0.05$; $n > 3$ each. (*G–J*) Fewer slowly dividing cells were seen in *galectin-1*-null mice than in wild-type mice. Slowly dividing cells in the SVZ were visualized as described in the legend of Fig. 2*B*. Dotted lines are drawn around the SVZ in *H* and *I*. (*J*) Significantly fewer long-term BrdU-retaining cells were observed in the SVZ of *galectin-1* mutant mice than in wild-type littermates. **, $P < 0.01$; $n > 3$ each. (Scale bars: 50 μm.)

anti-Galectin-1 neutralizing Ab (29) into the LV of adult wild-type mice significantly decreased the number of slowly dividing cells (Fig. 12, which is published as supporting information on the PNAS web site), a phenotype similar to that seen in *galectin-1*-null mutants (Fig. 4 *G–J*), suggesting that the endogenous Galectin-1 protein in the adult SVZ plays a role in the maintenance of neural progenitor cells. Moreover, the *galectin-1*-null mutation did not affect the number of apoptotic cells in the SVZ (Fig. 9 *C* and *D*). Together, these data suggest that Galectin-1 is required for the normal proliferation of type B and C cells in the adult brain.

The proliferation of adult and fetal NSCs is regulated by distinct mechanisms (41). Radial glial cells act as NSCs in the fetal and early postnatal brain and then may differentiate into astrocytes, expressing GFAP at approximately postnatal day (P) 7–15 (42, 43). Interestingly, Galectin-1 is not expressed before P9 in the FB (44). The brain of *galectin-1*-null mice at birth is indistinguishable from that of wild-type littermates (30, 45) except for an aberrant topography of olfactory axons (46). Therefore, Galectin-1 is most likely to play a role in adult NSCs rather than in embryonic NSCs. Taken together, our results demonstrate that Galectin-1 is expressed in slowly dividing SVZ astrocytes, which include the NSCs (34), and plays an important role in the proliferation of adult neural progenitor cells, including SVZ astrocytes. Stem cells reside in an area called a niche (47, 48), which has a characteristic cellular composition and signal mediators. In the niche, the state of each cell [i.e., cell cycle, apoptosis, and cell–cell or cell–extra cellular matrix (ECM) interactions] is strictly regulated to maintain stem cell homeostasis. Although ECM proteins are enriched in the SVZ (24, 49, 50), the niche for NSCs, the physiological significance of their carbohydrate structures has not been well characterized. In general, lectins exert their biological effects by binding to certain carbohydrate structures. Galectin-1's carbohydrate-binding ability is required for some functions but not others (27, 39, 51, 52). The present study suggests that the carbohydrate-binding activity of Galectin-1 is required for its promotion of adult neural progenitor cell proliferation. The analysis of Galectin-1 function will help us understand the important roles of carbohydrate molecules in stem cell biology, which may lead to the development of innovative therapies for human diseases.

Materials and Methods

Evaluation of OP9CM Activity. To assay the CM activity (see *Supporting Materials and Methods*, which is published as supporting information on the PNAS web site), neurospheres, prepared as described in ref. 53, were dissociated with trypsin and then FACS-sorted (*Supporting Materials and Methods*) at one cell per well directly into 96-well low-adhesion microtiter plates (Costar) containing each CM in a separate well. Human Galectin-1 was purchased from Genzyme Techne. To prepare the neurosphere CM (NSCM), neurospheres were cultured in the basal medium with 20 ng/ml human recombinant EGF (PeproTech, Rocky Hill, NJ) and FGF-2 (Genzyme Techne) for 48 h. To evaluate the activity of Galectin-1, the cells were sorted at 100 cells per well into NSCM-containing medium.

Molecular Identification of Galectin-1 in the CM. The OP9CM and IA-OP9CM preparations were analyzed by using the ProteinChip system (Ciphergen Biosystems). To screen the differences in peak heights, chemical surface chips that were positively charged, negatively charged, hydrophobic, C4, and Zn were used in the range of 500–200,000 Da. The affinity of the protein for each chip was monitored by using wash buffers of several pH values. To purify the 14.6-kDa protein, 200 ml of the OP9CM was freeze-dried, and a condensed solution was run on a Q-100 column (General Electric). The fraction that was eluted with 200 mM NaCl was used for SDS/PAGE. The 14.6-kDa band was cut from the gel and used for amino acid sequencing by tandem mass spectrometry.

Infusion into the SVZ and Adult Neurosphere Culture. Galectin-1 (2 or 14 μg), anti-Galectin-1 neutralizing Ab (rabbit IgG, 30 μg/ml, Kirin Brewery), or control rabbit IgG (30 μg/ml, Kirin Brewery) was dissolved in 0.9% saline with 1 mg/ml mouse serum albumin (Sigma) and infused into the LV as described in ref. 54 by using an osmotic pump (Alzet, Palo Alto, CA) at 0.5 μl/h for the given number of days. Adult neurosphere cultures from the infused brain samples were prepared as described in ref. 54.

Immunohistochemistry. Brains were perfusion-fixed with 4% paraformaldehyde (PFA) and postfixed in the same fixative overnight, and 50-μm sections were cut on a vibratome. Differentiated neurospheres grown on coverslips were immersion-fixed in 4% PFA for 15 min at room temperature. After three rinses in PBS, the neurospheres or sections were incubated for 1 h in TNB blocking solution (Vector Laboratories), incubated with primary antibodies overnight, and incubated for 60 min at room temperature with biotinylated secondary antibodies (1:200) or Alexa Fluor-conjugated secondary antibodies (1:200; Molecular Probes), unless otherwise noted. Biotinylated antibodies were visualized by using the Vectastain Elite ABC kit and TSA (Vector Laboratories). Anti-Galectin-1-neutralizing Abs were prepared as described in ref. 39. Other primary antibodies used in this study are described in *Supporting Materials and Methods*.

BrdU Labeling. For short-term labeling, after the intraventricular infusion of Galectin-1 for 7 days, mice received i.p. injections of BrdU (120 mg/kg dissolved in 0.007% NaOH in phosphate buffer; Sigma) every 2 h for 10 h and were killed 0.5 h after the last injection. For long-term labeling, 1 mg/ml BrdU was given to mice in their drinking water for 2 weeks (or 1 week in experiments involving the infusion of Galectin-1 or Abs). Mice were killed 10 or 30 days after the last day of infusion, and the brains were processed for immunohistochemistry.

Quantification of Histological Results. To quantify each cell type, 20 coronal vibratome sections of the SVZ (50 μm thick) were obtained at the level of the caudate-putamen (1.0–0 mm rostral to the bregma) from each hemisphere. The sections were stained for three different markers with BrdU (Sox21/BrdU, Dlx/BrdU, or Mash1/BrdU). Single confocal images were taken as 1-μm optical sections (LSM-510; Zeiss) from each vibratome section. The $BrdU^+$ nuclei that were positive for each marker (Sox21, Dlx, or Mash1) were counted, and the total number of $BrdU^+$ cells was multiplied by the ratio of the cells of each type to $BrdU^+$ cells, yielding the numbers for each cell type as follows: type B cells = total number of $BrdU^+$ [$(Sox21^+/BrdU^+)$ − $(Dlx^+/BrdU^+)$], type C cells = total number of $BrdU^+$ $(Mash1^+/BrdU^+)$, and type A cells = total number of $BrdU^+$ [$(Dlx^+/BrdU^+)$ − $(Mash1^+/BrdU^+)$]. The average number of each cell type per 50-μm section throughout the LV is indicated in each figure. Apoptotic cells were detected by using an ApoTag kit (Intergen, Purchase, NY). We quantified the cells in the LV contralateral to the infused side, because exposure to the increased concentration of reagent in the LV could have an artifactual effect.

Animals. For the adult mouse study, 8-week-old male mice were killed by anesthetic overdose. *galectin-1* knockout mice (129SJ background) are described in ref. 30. The animals were maintained on a 12-h light/12-h dark cycle with unlimited access to food and water. All experiments on live animals were performed in accordance with Keio University guidelines and regulations.

Statistical Analysis. Values are expressed as the mean ± SE. An unpaired *t* test (for two groups) or ANOVA with the Bonferroni correction (for more than three groups) was used to evaluate the differences of the averages, unless otherwise noted.

We thank K. Sakurada, S. Kaneko, Masatake Osawa, H. Miyoshi, K. Nakashima, T. Imai, and S. Yamanaka for critical advice; T. Nakano (Osaka University, Japan), T. Kitamura (University of Tokyo), T. Seki (Juntendo University, Tokyo), H. Ohba (Keio University), K. Adachi (Keio University), O. Yamada (Keio University), and G. Panganiban (University of Wisconsin, Madison) for experimental materials; R. Wakatabe, Y. Fukase, Mitsujiro Osawa, Y. Morita, T. Yamashita, K. Sango, S. Kuno, Y. Hayakawa, and Y. Fujita for technical assistance; M. Ito, K. Inoue, and A. Hirayama for secretarial assistance; and S. Sakaguchi for critical advice and continuous support. This work was supported by grants from the Ministry of Education, Culture, Sports, Science, and Technology of Japan (MEXT); Core Research for Evolutional Science and Technology of the Japan Society and Technology Agency (to H. Okano); the 21st Century Centers of Excellence Program of MEXT (to Keio University and Tokyo Medical and Dental University); Association pour la Recherche sur le Cancer, Lingue Nationale Française Contre le Cancer, and Association Française Contre les Myopathies (to F.P.); and the National Institutes of Health and National Institute of Neurological Disorders and Stroke (to M. Sakaguchi).

1. Alvarez-Buylla, A. & Lim, D. A. (2004) *Neuron* **41,** 683–686.
2. Okano, H. (2002) *J. Neurosci. Res.* **69,** 698–707.
3. Lie, D. C., Song, H., Colamarino, S. A., Ming, G. L. & Gage, F. H. (2004) *Annu. Rev. Pharmacol. Toxicol.* **44,** 399–421.
4. Lois, C. & Alvarez-Buylla, A. (1993) *Proc. Natl. Acad. Sci. USA* **90,** 2074–2077.
5. Levison, S. W. & Goldman, J. E. (1993) *Neuron* **10,** 201–212.
6. Luskin, M. B. (1993) *Neuron* **11,** 173–189.
7. Altman, J. & Das, G. D. (1965) *J. Comp. Neurol.* **124,** 319–335.
8. Bayer, S. A., Yackel, J. W. & Puri, P. S. (1982) *Science* **216,** 890–892.
9. Eriksson, P. S., Perfilieva, E., Bjork-Eriksson, T., Alborn, A. M., Nordborg, C., Peterson, D. A. & Gage, F. H. (1998) *Nat. Med.* **4,** 1313–1317.
10. van Praag, H., Schinder, A. F., Christie, B. R., Toni, N., Palmer, T. D. & Gage, F. H. (2002) *Nature* **415,** 1030–1034.
11. Carleton, A., Petreanu, L. T., Lansford, R., Alvarez-Buylla, A. & Lledo, P. M. (2003) *Nat. Neurosci.* **6,** 507–518.
12. Gheusi, G., Cremer, H., McLean, H., Chazal, G., Vincent, J. D. & Lledo, P. M. (2000) *Proc. Natl. Acad. Sci. USA* **97,** 1823–1828.
13. Nakatomi, H., Kuriu, T., Okabe, S., Yamamoto, S., Hatano, O., Kawahara, N., Tamura, A., Kirino, T. & Nakafuku, M. (2002) *Cell* **110,** 429–441.
14. Reya, T., Morrison, S. J., Clarke, M. F. & Weissman, I. L. (2001) *Nature* **414,** 105–111.
15. Takakura, N., Kodama, H. & Nishikawa, S. (1996) *J. Exp. Med.* **184,** 2301–2309.
16. Ueno, H., Sakita-Ishikawa, M., Morikawa, Y., Nakano, T., Kitamura, T. & Saito, M. (2003) *Nat. Immunol.* **4,** 457–463.
17. Reynolds, B. A. & Weiss, S. (1992) *Science* **255,** 1707–1710.
18. Fung, E. T., Thulasiraman, V., Weinberger, S. R. & Dalmasso, E. A. (2001) *Curr. Opin. Biotechnol.* **12,** 65–69.
19. Teichberg, V. I., Silman, I., Beitsch, D. D. & Resheff, G. (1975) *Proc. Natl. Acad. Sci. USA* **72,** 1383–1387.
20. Barondes, S. H., Castronovo, V., Cooper, D. N., Cummings, R. D., Drickamer, K., Feizi, T., Gitt, M. A., Hirabayashi, J., Hughes, C., Kasai, K., *et al.* (1994) *Cell* **76,** 597–598.
21. Perillo, N. L., Marcus, M. E. & Baum, L. G. (1998) *J. Mol. Med.* **76,** 402–412.
22. Leffler, H. (2001) *Results Probl. Cell Differ.* **33,** 57–83.
23. Capela, A. & Temple, S. (2002) *Neuron* **35,** 865–875.
24. Mercier, F., Kitasako, J. T. & Hatton, G. I. (2002) *J. Comp. Neurol.* **451,** 170–188.
25. Yanagisawa, M., Liour, S. S. & Yu, R. K. (2004) *J. Neurochem.* **91,** 804–812.
26. Pipia, G. G. & Long, M. W. (1997) *Nat. Biotechnol.* **15,** 1007–1011.
27. Vas, V., Fajka-Boja, R., Ion, G., Dudics, V., Monostori, E. & Uher, F. (2005) *Stem Cells* **23,** 279–287.
28. Tropepe, V., Sibilia, M., Ciruna, B. G., Rossant, J., Wagner, E. F. & van der Kooy, D. (1999) *Dev. Biol.* **208,** 166–188.
29. Horie, H., Inagaki, Y., Sohma, Y., Nozawa, R., Okawa, K., Hasegawa, M., Muramatsu, N., Kawano, H., Horie, M., Koyama, H., *et al.* (1999) *J. Neurosci.* **19,** 9964–9974.
30. Poirier, F. & Robertson, E. J. (1993) *Development (Cambridge, U.K.)* **119,** 1229–1236.
31. Joubert, R., Kuchler, S., Zanetta, J. P., Bladier, D., Avellana-Adalid, V., Caron, M., Doinel, C. & Vincendon, G. (1989) *Dev. Neurosci.* **11,** 397–413.
32. Brown, D. C. & Gatter, K. C. (1990) *Histopathology* **17,** 489–503.
33. Seri, B., Garcia-Verdugo, J. M., McEwen, B. S. & Alvarez-Buylla, A. (2001) *J. Neurosci.* **21,** 7153–7160.
34. Doetsch, F., Caille, I., Lim, D. A., Garcia-Verdugo, J. M. & Alvarez-Buylla, A. (1999) *Cell* **97,** 703–716.
35. Parras, C. M., Galli, R., Britz, O., Soares, S., Galichet, C., Battiste, J., Johnson, J. E., Nakafuku, M., Vescovi, A. & Guillemot, F. (2004) *Embo. J.* **23,** 4495–4505.
36. Doetsch, F., Petreanu, L., Caille, I., Garcia-Verdugo, J. M. & Alvarez-Buylla, A. (2002) *Neuron* **36,** 1021–1034.
37. Morshead, C. M., Reynolds, B. A., Craig, C. G., McBurney, M. W., Staines, W. A., Morassutti, D., Weiss, S. & van der Kooy, D. (1994) *Neuron* **13,** 1071–1082.
38. Whitney, P. L., Powell, J. T. & Sanford, G. L. (1986) *Biochem. J.* **238,** 683–689.
39. Inagaki, Y., Sohma, Y., Horie, H., Nozawa, R. & Kadoya, T. (2000) *Eur. J. Biochem.* **267,** 2955–2964.
40. Yu, C. C. & Filipe, M. I. (1993) *Histochem. J.* **25,** 843–853.
41. Shi, Y., Chichung Lie, D., Taupin, P., Nakashima, K., Ray, J., Yu, R. T., Gage, F. H. & Evans, R. M. (2004) *Nature* **427,** 78–83.
42. Tramontin, A. D., Garcia-Verdugo, J. M., Lim, D. A. & Alvarez-Buylla, A. (2003) *Cereb. Cortex* **13,** 580–587.
43. Alvarez-Buylla, A., Garcia-Verdugo, J. M. & Tramontin, A. D. (2001) *Nat. Rev. Neurosci.* **2,** 287–293.
44. Poirier, F., Timmons, P. M., Chan, C. T., Guenet, J. L. & Rigby, P. W. (1992) *Development (Cambridge, U.K.)* **115,** 143–155.
45. Colnot, C., Fowlis, D., Ripoche, M. A., Bouchaert, I. & Poirier, F. (1998) *Dev. Dyn.* **211,** 306–313.
46. Puche, A. C., Poirier, F., Hair, M., Bartlett, P. F. & Key, B. (1996) *Dev. Biol.* **179,** 274–287.
47. Schofield, R. (1978) *Blood Cells* **4,** 7–25.
48. Spradling, A., Drummond-Barbosa, D. & Kai, T. (2001) *Nature* **414,** 98–104.
49. Campos, L. S., Leone, D. P., Relvas, J. B., Brakebusch, C., Fassler, R., Suter, U. & Ffrench-Constant, C. (2004) *Development (Cambridge, U.K.)* **131,** 3433–3444.
50. Emsley, J. G. & Hagg, T. (2003) *Exp. Neurol.* **183,** 273–285.
51. Liu, F. T. & Rabinovich, G. A. (2005) *Nat. Rev. Cancer* **5,** 29–41.
52. Wells, V. & Mallucci, L. (1991) *Cell* **64,** 91–97.
53. Shimazaki, T., Shingo, T. & Weiss, S. (2001) *J. Neurosci.* **21,** 7642–7653.
54. Shingo, T., Gregg, C., Enwere, E., Fujikawa, H., Hassam, R., Geary, C., Cross, J. C. & Weiss, S. (2003) *Science* **299,** 117–120.

nature medicine

Conditional ablation of Stat3 or Socs3 discloses a dual role for reactive astrocytes after spinal cord injury

Seiji Okada[1–3], Masaya Nakamura[4], Hiroyuki Katoh[4], Tamaki Miyao[1], Takuya Shimazaki[1], Ken Ishii[4], Junichi Yamane[1,4], Akihiko Yoshimura[5], Yukihide Iwamoto[2], Yoshiaki Toyama[4] & Hideyuki Okano[1,3]

In the injured central nervous system (CNS), reactive astrocytes form a glial scar and are considered to be detrimental for axonal regeneration, but their function remains elusive. Here we show that reactive astrocytes have a crucial role in wound healing and functional recovery by using mice with a selective deletion of the protein signal transducer and activator of transcription 3 (Stat3) or the protein suppressor of cytokine signaling 3 (Socs3) under the control of the *Nes* promoter-enhancer (*Nes-Stat3*$^{-/-}$, *Nes-Socs3*$^{-/-}$). Reactive astrocytes in *Nes-Stat3*$^{-/-}$ mice showed limited migration and resulted in markedly widespread infiltration of inflammatory cells, neural disruption and demyelination with severe motor deficits after contusive spinal cord injury (SCI). On the contrary, we observed rapid migration of reactive astrocytes to seclude inflammatory cells, enhanced contraction of lesion area and notable improvement in functional recovery in *Nes-Socs3*$^{-/-}$ mice. These results suggest that Stat3 is a key regulator of reactive astrocytes in the healing process after SCI, providing a potential target for intervention in the treatment of CNS injury.

Because the regenerative capability of the mammalian CNS is poor, limited functional recovery occurs during the chronic phase of SCI. At the subacute phase of SCI, however, gradual functional recovery is observed to some extent in both rodents and humans (except in cases of complete paralysis). The mechanism behind this functional recovery remains unclear. Here, we investigated this issue by focusing on the action of reactive astrocytes in a mouse model of SCI.

To interpret the process of paralysis improvement in the subacute phase, we examined serial histological sections of contused spinal cords and followed motor function for 6 weeks after injury in wild-type mice and found that the area of neural cell loss gradually enlarged in a rostral-caudal direction within a few days after SCI (acute phase) and a portion of Hu-expressing neurons were positive for cleaved caspase-3, indicating that the secondary injury process lasted for several days in this model (**Supplementary Fig. 1** online) during which we observed limited functional recovery (**Fig. 1a**). Astrocytes surrounding the lesion underwent a typical change of hypertrophy, process extension and increased expression of intermediate filaments such as GFAP and Nestin by 7 d after SCI (**Fig. 1b**), characteristic of 'reactive astrocytes.' Notably, these astrocytes eventually migrated centripetally to the lesion epicenter and gradually compacted the CD11b^{+} inflammatory cells, contracting the lesion area up until 14 d after SCI (subacute phase; **Fig. 1c,d**). During this process, we observed repair of injured tissue and gradual functional improvement, and reactive astrocytes formed a physical barrier against inflammatory cells, commonly referred to as glial scar. After the migration of reactive astrocytes and completion of glial scar (reactive gliosis), functional improvement reached a plateau around 2 weeks after injury (**Fig. 1a,c**). Although the glial scar has a crucial part in the lack of axonal regeneration in the chronic phase of SCI[1], our data strongly suggest that the emergence and migration of reactive astrocytes have a prominent role in the repair of injured tissue and the restoration of motor function in the subacute phase (before completion of the glial scar).

To confirm that the compaction of the lesion results from migration and not from proliferation of reactive astrocytes, we labeled proliferating cells with bromodeoxyuridine (BrdU). Analysis of mice that received a single injection of BrdU at 7 d after SCI showed that the population of BrdU^{+} cells was composed of reactive astrocytes and inflammatory cells, which were gradually compacted to the lesion center as time progressed (**Fig. 1e** and **Supplementary Fig. 2** online). Analysis of mice that received daily injections of BrdU showed limited astrocyte proliferation after 7 d postinjury, suggesting that the development of reactive gliosis is mainly brought about by cellular hypertrophy and upregulation of GFAP of the astrocytes surrounding the lesion (**Fig. 1f,g**).

To address the regulatory mechanisms behind the reactive response of astrocytes, we investigated the role of Stat3 signaling (**Figs. 2** and **3**). Stat3 is a principal mediator in a variety of biological processes[2–4] including cancer progression, wound healing and the movement of various types of cells. In addition, Stat3 mediates certain aspects of astrogliosis downstream of the action of cytokines such as interleukin (IL)-6, leukemia inhibitory factor (LIF) and ciliary neurotrophic factor (CNTF) after CNS injury[5–8].

[1]Department of Physiology, Keio University School of Medicine, 35 Shinanomachi, Shinjuku-ku, Tokyo 160-8582, Japan. [2]Department of Orthopaedic Surgery, Graduate School of Medical Sciences, Kyushu University, 3-1-1 Maidashi, Higashi-ku, Fukuoka 812-8582, Japan. [3]Core Research for Evolutional Science and Technology (CREST), Japan Science and Technology, 4-1-8 Honcho, Kawaguchi, Saitama 332-0012, Japan. [4]Department of Orthopaedic Surgery, Keio University School of Medicine, 35 Shinanomachi, Shinjuku-ku, Tokyo 160-8582, Japan. [5]Division of Molecular and Cellular Immunology, Medical Institute of Bioregulation Graduate School of Medical Sciences, Kyushu University, 3-1-1 Maidashi, Higashi-ku, Fukuoka 812-8582, Japan. Correspondence should be addressed to H.O. (hidokano@sc.itc.keio.ac.jp).

Received 8 November 2005; accepted 28 April 2006; published online 18 June 2006; doi:10.1038/nm1425

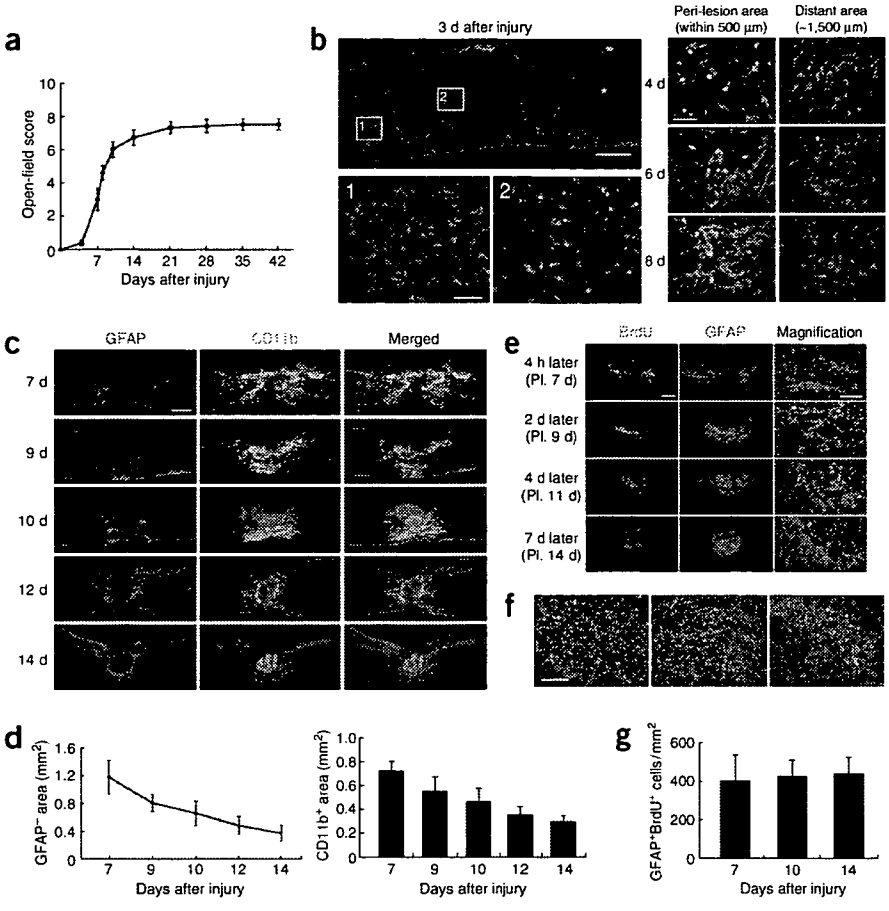

Figure 1 Migration of reactive astrocytes and compaction of inflammatory cells in wild-type mice. (**a**) Time course of lower limb functional recovery after SCI ($n = 10$). There was gradual recovery in the subacute phase. Data are mean ± s.e.m. (**b**) Phosphorylated Stat3 (green) and morphological changes were observed in GFAP$^+$ astrocytes (red) close to the lesion (boxed area 2) but not in distant areas (boxed area 1) at 3, 4, 6 and 8 d after SCI. Scale bar, 500 μm (upper left panel), 100 μm (lower left panel) and 50 μm (right panels). Asterisk indicates the lesion epicenter. (**c**) Time course of GFAP$^+$ reactive astrocytes and CD11b$^+$ cells. Reactive astrocytes gradually confine the area of inflammatory cell infiltration. Scale bar, 500 μm. (**d**) Quantitative analysis of GFAP$^-$ area (surrounded by reactive astrocytes) and CD11b$^+$ area ($n = 3$ per each time point). Data are mean ± s.d. (**e**) BrdU-labeled cells migrated toward the lesion epicenter. Mice were injected with BrdU (100 μg/g body weight) at 7 d after injury and killed 4 h, 2 d, 4 d, 7 d later. Scale bar, 500 μm and 100 μm. (**f**) The proliferating reactive astrocytes were labeled by daily injection of BrdU from the day of injury till killing at 7 (left), 10 (middle) and 14 d (right) after injury. GFAP, red; BrdU, green. Scale bar, 100 μm. (**g**) There were no differences in the number of GFAP$^+$BrdU$^+$ cells from 7 to 14 d after injury ($n = 3$ per group). Data are mean ± s.d.

In the injured spinal cord, phosphorylated Stat3 prominently increased at 12 h after injury, which remained detectable for 2 weeks (**Fig. 3a**). We observed phosphorylation and nuclear translocation of Stat3 mainly in reactive astrocytes surrounding the lesion, but not in distant areas for several days after injury (**Fig. 1b** and **Supplementary Fig. 1**). To elucidate the role of Stat3 in reactive astrocytes, we selectively disrupted the *Stat3* gene under the control of *Nes* gene promoter and second intronic enhancer, which are activated in reactive astrocytes after SCI[9,10]. We created conditional knockout mice (*Nes-Stat3*$^{-/-}$) by crossing *Stat3*^{loxP} mice[11] with *Nes*-Cre transgenic mice[12], as embryonic lethality ensues in Stat3-null mice. *Nes-Stat3*$^{-/-}$ mice showed no apparent abnormalities in motor function and development, although they showed signs of hyperphagia and leptin resistance[13]. To identify the cells that underwent Cre-mediated recombination, we crossed another transgenic line[14] carrying a reporter gene construct, *CAG* promoter-*lox*P-CAT-*lox*P-EGFP (CAG-CAT$^{loxP/loxP}$-EGFP), which directs the expression of EGFP upon Cre-mediated recombination. After SCI, we observed high Cre-mediated expression of EGFP from reactive astrocytes surrounding the lesion, but not from neurons or oligodendrocytes (**Supplementary Figs. 3** and **4** online), indicating recombination only in reactive astrocytes in both littermates and *Nes-Stat3*$^{-/-}$ mice.

At 2 weeks after injury, *Nes-Stat3*$^{-/-}$ mice showed markedly widespread infiltration of CD11b$^+$ inflammatory cells and demyelination compared to wild-type littermates (**Fig. 2a**). Notably, although the development of glial scar was observed around the injury site several days after injury in *Nes-Stat3*$^{-/-}$ mice (**Fig. 2a,b** and **Supplementary Fig. 3**), the configuration of these cells remained relatively unchanged for the following 6 weeks owing to their limited migration, resulting in widespread demyelination and severe motor deficits (**Fig. 2**). Quantifications of GFAP$^-$ area and CD11b$^+$ area in wild-type littermates and *Nes-Stat3*$^{-/-}$ mice were comparable at 7 d after injury, implying a similar degree of astrocyte loss owing to secondary injury, but marked differences developed during the following 7 d, suggesting that Stat3 has a large impact on the migration of astrocytes rather than their survival after SCI (**Fig. 2c**). The progressive compaction of GFAP$^+$EGFP$^+$ cells toward the lesion center observed in wild-type littermates did not occur in *Nes-Stat3*$^{-/-}$ mice, providing further evidence of Stat3-dependent migration of reactive astrocytes (**Fig. 2d**). Confocal imaging confirmed the emergence of reactive astrocytes without phosphorylated Stat3 in *Nes-Stat3*$^{-/-}$ mice (**Fig. 2e**), indicating that the Stat3 activation is not necessarily indispensable for the appearance of reactive astrocytes or for the upregulation of *Gfap* and *Nes*. These data suggest that Stat3 is a key molecule for the migratory function of reactive astrocytes, which may be deeply involved in tissue repair and functional recovery after SCI (**Fig. 2**).

To further investigate the relationship between Stat3 signaling and function of reactive astrocytes, we analyzed SCI in *Nes-Socs3*$^{-/-}$ mice[15]. Socs3 is the negative feedback molecule of Stat3 and the 'bipolar' relationship between Stat3 and Socs3 has been noted in several selective deletion experiments[13,15,16]. In the injured spinal cord of *Nes-Socs3*$^{-/-}$ mice, phosphorylation of Stat3 was significantly greater and prolonged compared to that in wild-type mice, and immunohistochemistry confirmed greater expression of phosphorylated Stat3 in reactive astrocytes (**Fig. 3a–c**). Notably, the rapid development of reactive gliosis that compacted inflammatory cells in the injured spinal cord of *Nes-Socs3*$^{-/-}$ mice was observed as early as 7 d after injury (**Fig. 3d,e**). GFAP$^-$ area and CD11b$^+$ area were significantly reduced in *Nes-Socs3*$^{-/-}$ mice at 7 d after injury, during which *Nes-Socs3*$^{-/-}$ mice showed marked improvement of motor function compared to littermates (**Fig. 3f,g**). The differences in the area between wild-type